Simulation Algorithms for Inductive Effects

by

Yehia Mahmoud Massoud

B.S. Electronics Engineering, Cairo University, Egypt (1991)
M.S. Electronics Engineering, Cairo University, Egypt (1994)

Submitted to the Department of Electrical Engineering and Computer Science
in partial fulfillment of the requirements for the degree of

Doctor of Philosophy

at the

MASSACHUSETTS INSTITUTE OF TECHNOLOGY

September 1999

© 1999 Massachusetts Institute of Technology

Signature of Author⎯⎯⎯⎯⎯⎯⎯⎯⎯⎯⎯⎯⎯⎯⎯⎯⎯⎯⎯⎯⎯⎯⎯⎯⎯⎯⎯⎯⎯⎯
Department of Electrical Engineering and Computer Science
August 31, 1999

Certified by⎯⎯⎯⎯⎯⎯⎯⎯⎯⎯⎯⎯⎯⎯⎯⎯⎯⎯⎯⎯⎯⎯⎯⎯⎯⎯⎯⎯⎯⎯⎯⎯
Jacob K. White
Professor of Electrical Engineering and Computer Science
Thesis Supervisor

Accepted by⎯⎯⎯⎯⎯⎯⎯⎯⎯⎯⎯⎯⎯⎯⎯⎯⎯⎯⎯⎯⎯⎯⎯⎯⎯⎯⎯⎯⎯⎯⎯⎯
Arthur C. Smith
Chairman, Departmental Committee on Graduate Students

Simulation Algorithms for Inductive Effects

by

Yehia Mahmoud Massoud

Submitted to the Department of Electrical Engineering and Computer Science
on August 31, 1999, in partial fulfillment of the
requirements for the degree of
Doctor of Philosophy

Abstract

Advancement in VLSI and MEMS technologies necessitates accurate prediction of inductive effects. In the VLSI world, ever increasing VLSI circuit speeds pose challenges for accurate modeling of on-chip inductive effects and their effects on circuit performance. In this scenario, minimizing inductive effects is a challenging issue. Additionally, in the MEMS field, several new MEMS designs generate large forces using magnetic fields combined with highly permeable materials. Accurate and efficient inductance solvers are essential for the analysis and developments of such devices.

This thesis describes several algorithms for accurate simulation of inductive effects. Part I deals with the analysis of on-chip interconnect inductive effects. It first investigates the interconnect coupling inductance and its effect on circuit crosstalk. The effect of the finite conductivity semiconductor substrates on inductive coupling and signal integrity is simulated. Limitations of standard approaches for estimating coupling inductance are examined. A method for the reduction of the coupling inductance is also proposed. Part I then analyzes the minimization of the interconnect self inductance, and therefore, reducing its effect on signal delay and delay skew. Different techniques for reducing interconnect self inductance are compared. The proposed less area-consuming technique with very little area penalty are more effective at minimizing self-inductance than the commonly used dedicated ground planes technique.

In the second part of the thesis, a fast algorithm to efficiently extract the frequency dependent inductance for 3-D structures that contain permeable materials is developed. The method uses a magnetic surface charge formulation, with very efficient techniques for evaluating the required integrals. This approach avoids numerical cancellation errors by calculating fields outside of the permeable material. The resulting system is solved iteratively using a preconditioned GMRES method to allow the analysis of complicated structures.

Thesis Supervisor: Jacob K. White
Title: Professor of Electrical Engineering and Computer Science

Acknowledgments

First and foremost, I would like to acknowledge the continuous encouragement and support I received from my thesis advisor, Professor Jacob White. It has been an honor and a privilege to work with Jacob. His extreme enthusiasm behind the project and his valuable advice is all reflected on this thesis.

I would also like to thank my thesis committee members, Professors Steve Senturia and Steve Leeb for their willingness to evaluate this work and for their valuable comments and suggestions.

I am grateful to the staff of the Motorola's Somerset design center for their hospitality. Most of the work for Chapter 3 was performed there. In particular Steve Majors and Tareq Bustami contributed greatly to this work.

I am indebted to all the members of RLE-VLSI at MIT group, in particular, Matt Kamon, Junfeng Wang, Deepak Ramaswamy, and Jurgen Singer for their help and friendship.

I am also indebted to all members of DARPA magnetics project for the interesting and fruitful discussions during the group meetings.

On a more personal note, I would like to thank my mother Amina, my father Mahmoud, and my sister Samya for all their continuous love and encouragement throughout these years. I would also like to thank God for giving me a cute daughter, Samya, who brought lots of joy to my life. Finally, this work would not have been possible without the extreme patience and encouragement of my wife, Zahra.

Say: are they equal,

those who know and those who don't know ?

> *– The Glorious Koran*
>
> *(39:9)*

Not only to say the right thing in the right place,

but far more difficult, to leave unsaid the wrong

thing at the tempting moment.

> *– George Sala*

To my parents Amina and Mahmoud,

my wife Zahra and daughter Samya.

Contents

II　Inductance Extraction for Structures that Contain Permeable Materials　51

9

List of Figures

13

List of Tables

1

Introduction

Inductance modeling and inductive effects simulation are becoming very important factors in the design and analysis of VLSI circuits and microelectromechanical devices (MEMS).

The design process of high performance microprocessors is being increasingly impacted by inductive effects [1]. This was forecasted by well known technology trends [2]. The rapid rate of process technology advancements and heightening market pressures for functional integration are resulting in larger VLSI chips operating at steadily increasing frequencies. The adverse effect of these developments is the increase in the on-chip interconnect inductance, and consequently, increase in signal delay and circuit crosstalk. Interconnect lines with larger inductance will display increased sensitivity to distant variations in interconnect topology, since magnetic effects have a much longer spatial range than electrostatic effects. Prediction of on-chip inductance and its effect on circuit performance is difficult because of this long range sensitivity

Until recently, the semiconductor substrate was commonly assumed to be a proximate ideal ground plane and based on this theory, on-chip coupling inductance was assumed to be negligible. Utilizing this ideal ground plane assumption has led to simplistic models for the coupling inductance between interconnect lines, which predict small coupling inductance. Additionally, most delay analysis tools do not model interconnect self inductance, and are limited to RC networks leaving an inherent unpredictability in the design

process where inductive effects are suspected.

Permeable materials have been used in many of today's MEMS devices such as, micromotors [3], planar inductors [4, 5, 6, 7, 8], and magnetic force based actuators [9, 10, 11, 12, 13] to increase the device's inductance, and consequently, the force generated by the device. Permeable materials have been also used in magnetic micro power applications to miniaturize various electronic devices including inductors and transformers [14, 15, 16, 17, 18, 19].

A common approach to extract the inductance for these structures is to apply a finite difference or finite element method to the governing equations in differential form. Such an approach generates a global mesh for all parts of analyzed structure and for surrounding external space. This causes the number of unknowns to increase significantly, and thus, a very large linear system can be generated, as shown in Figure 1-1. Solving this large generated linear system requires excessive memory, and consumes long CPU time which makes the analysis of complex 3-D permeable structures impractical.

Additionally, most of the approaches that compute the magnetic field for structures that contain permeable materials assume the uniformity of the current distribution across the cross section of the current carrying conductors. This assumption is only valid at very low frequencies, which makes it impractical to be used with the steadily increasing operating frequencies.
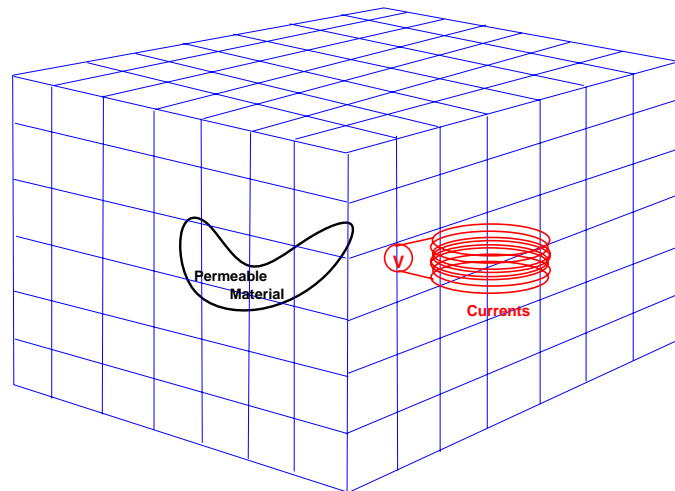
FIGURE 1-1: Finite difference discretization of all of space

Part I of this thesis investigates on-chip inductance. In Chapter 2, we investigate the interconnect coupling inductance and its effect on circuit crosstalk. In order to examine the accuracy of the standard ideal ground plane assumption, we simulated the semiconductor using a full 3-D mesh of filaments, and extended the 3-D inductance extraction program Fasthenry to include finite conductivity volume ground planes. We then used that capability to more accurately model the semiconductor substrates, and its effect on coupling inductance. In Chapter 2, we also investigate the effect of the on-chip inductive coupling on circuit cross-talk. In addition, the limitations of standard approaches for estimating coupling inductance are examined. A method for the reduction of the coupling inductance is also discussed.

Chapter 3 deals with interconnect self inductance. A highly effective method for minimizing self inductance without increasing die area has been demonstrated. This approach can be used to help constrain a design to the RC domain to maintain predictability at some performance cost, or it can be used as a basis for alternative design rules where inductance and capacitance must be traded off to optimize for specific performance targets.

In part II of this thesis, we develop a fast algorithm to efficiently extract the frequency dependant inductance in presence of linear permeable materials. The approach used is based on including fictitious magnetic surface charges. This method avoids computing fields inside the permeable materials, as these small fields are difficult to compute accurately due to numerical cancellation errors. In Chapter 4, we derive the integral formulation and then, in Chapter 5, we show how the individual integrals in the integral formulation are efficiently evaluated. In Chapter 5, we describe computational experiments that demonstrate the validity and accuracy of our formulation by comparing the numerically computed results to analytically derived results and published data. In Chapter 6, we show different examples which exhibit frequency dependent inductance, and we also show the variation of inductance with permeability. We also show how the resulting linear system can be solved iteratively using a preconditioned GMRES method. Finally, in Chapter 7, we summarize the work done in thesis and discuss possible extensions of

the algorithms presented.

Many of the sections of this thesis also exist in published form. some of Part I appears in [20, 21, 22, 23, 24]. All of part II (Chapters 4, 5, and 6) is implemented in C code available from `ftp://rle-vlsi.mit.edu/pub/fastmag`. Sections of Part II appear in [25, 26, 27].

Part I

Minimizing On-Chip Inductive Effects

In this part of the thesis, we analyze on-chip inductive effects and explore methods to minimize these effects. In Chapter 2, we investigate the interconnect coupling inductance and its effect on circuit crosstalk. In order to examine the accuracy of the standard ideal ground plane assumption, we extended the 3-D inductance extraction program Fasthenry to include finite conductivity volume ground planes. We then used that capability to more accurately model the semiconductor substrates and its effect on coupling inductance. In section 2.2, we briefly describe the standard technique to model the semiconductor substrate. In section 2.3, we briefly describe the Fasthenry program and our modifications. In Section 2.4, we show the simulated frequency dependant coupling inductance, and then in section 2.5, we discuss the limitations on the standard approach. In section 2.6, we show the effect of the inductive coupling on some circuits with different technologies. Finally in section 2.7, we discuss a method for the reduction of the coupling inductance and its effect on circuit crosstalk.

Chapter 3 deals with interconnect self inductance and demonstrates a highly effective method for minimizing self inductance without increasing die area. In section 3.2, we examine the inductance of a signal line sandwiched between ground return lines and show that line spacing can have only a limited impact on self-inductance. In section 3.3, we use three-dimensional magnetoquasistatic analysis to show that for integrated circuit interconnect operating at below twenty-five gigahertz, it is the low frequency inductance that predicts performance[3]. In section 3.4, we compare the performance of the sandwiched structure, using two dedicated ground planes and interdigitating thinned signal lines with thinned ground lines. Results in section 3.4 demonstrate that the interdigitated approach reduces self-inductance by more than a factor of four over the other techniques, for a modest rise in capacitance, resistance and area.

<div align="right">

2

</div>

Effect of Substrate Conductivity on Coupling Inductance and Signal Integrity

2.1 Motivation

In order to understand the effect of interconnect coupling inductance on circuit crosstalk, consider the example of a pair of parallel interconnect lines over a semiconductor substrate driving two inverters , as shown in Figure 2-1. While one of the lines, is switching the other line is quiet. Due to the inductive coupling between the two lines, the quiet line will exhibit a voltage glitch on it. This voltage glitch can produce wrong logic and thus circuit failure. This makes it very important to accurately simulate the effect of the coupling inductance on circuit crosstalk.

2.2 Standard Approach for Computing Coupling Inductance

It is commonly assumed that on-chip inductive coupling effects are negligible, and this assumption is based on the presumption that the semiconductor substrate is a proximate ideal ground plane. For example, using the ideal ground plane assumption leads to a
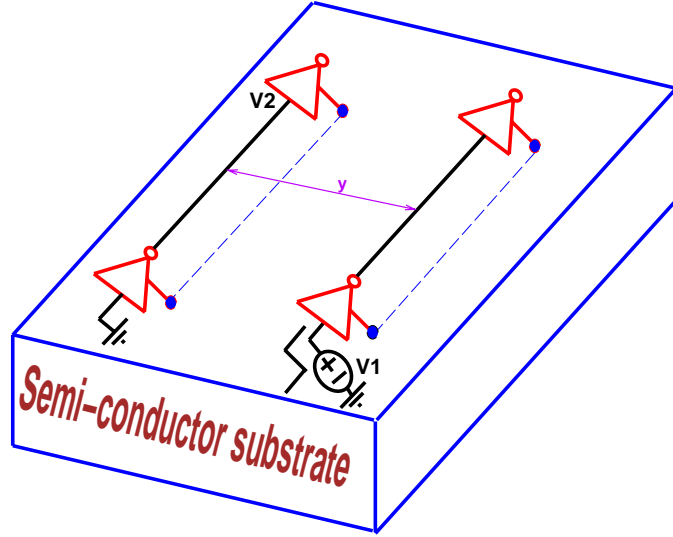
FIGURE 2-1: Two long interconnect lines running over a semiconductor substrate

simple model for the coupling inductance between parallel interconnect lines. A pair of parallel lines of length l, with a separation distance y and height above the ground plane $\frac{1}{2}z$ can be represented, using the method of images, as the two loop structure shown in Figure 2-3. Two-dimensional analysis [28] of the structure leads to a simple formula for the coupling inductance,

$$ L = \frac{\mu_0 l}{\pi} \ln \frac{\sqrt{y^2 + z^2}}{y}, \tag{2.1} $$

where l, z and y are the loop length, height and separation respectively, as defined in Figure 2-3. Figure 2-4 verifies that equation (2.1) is accurate for the two-loop model when $l > y$.

2.3   Simulating Substrates using 3-D Ground Planes

In order to capture the current distribution and the skin effect in the semiconductor substrate, we simulated the semiconductor using a full 3-D mesh of filaments. We extended the 3-D inductance extraction program Fasthenry [29] to simulate 3-D ground planes.

Fasthenry uses a standard filament discretization of an integral formulation of mag-
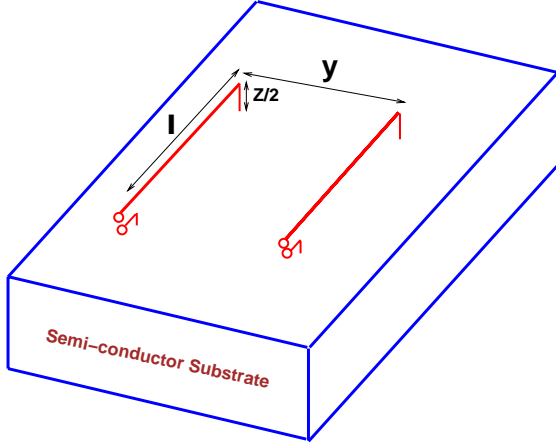
FIGURE 2-2: Two conductors over a semi-conductor substrate
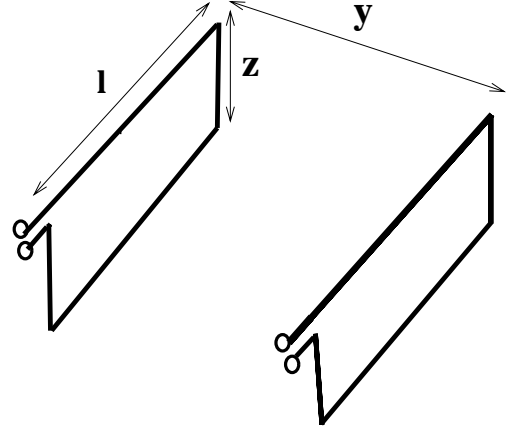
FIGURE 2-3: Simple two-loop coupling inductance model.
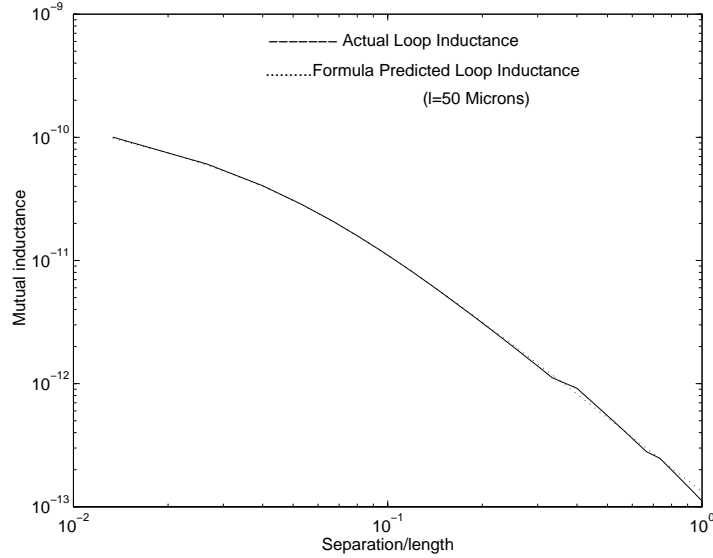
FIGURE 2-4: Comparison between the inductance predicted by equation (2.1) and actual inductance for the two loop model

netoquasistatic coupling [30]. The integral equation is

$$\frac{J(r)}{\sigma} + \frac{jw\mu}{4\pi} \int_{V'} \frac{J(r')}{|r - r'|} dv' = -\nabla \Phi(r), \qquad (2.2)$$

where Φ is referred to as the scalar potential, and V' is the volume of all conductors.

Then, by simultaneously solving (2.2) with the current conservation equation,

$$\nabla \cdot J = 0, \qquad (2.3)$$

conductor current densities, J, and the scalar potential can be computed. In Fasthenry,
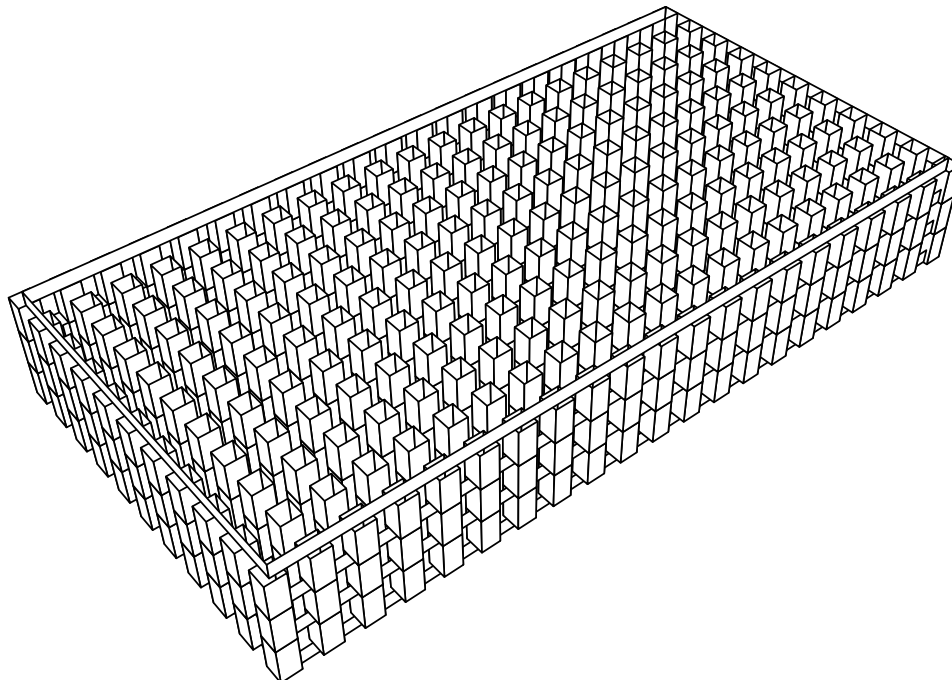
FIGURE 2-5: Substrate volume filament-based discretization.

a mesh formulation of the discretized equation is used to generate a dense system of equations which is solved iteratively using the fast multipole algorithm [31, 32]. In order to examine the impact of the finite conductivity of the semiconductor substrate ground plane, a volume filament discretization [33] for the semiconductor substrate was added to the Fasthenry program, as shown in Figure 2-5. The volume filament discretization for the substrate was constructed by first laying down a three dimensional grid of nodes, and then with filaments, connecting each node to its adjacent nodes excluding diagonally adjacent ones, as shown in Figure 2-6. Filament cross sections are chosen such that no space is left between parallel adjacent filaments.

2.4   Coupling Inductance Behavior

In this section, we examine the impact of the semiconductor substrate conductivity on coupling inductance. For the simulation examples below, the cross section of the conductors is 1μ by 1μ, reasonable for current DRAM technology [34]. The conductors were also chosen to be 100μ long, 1μ above the substrate, and have 2μ separation distance
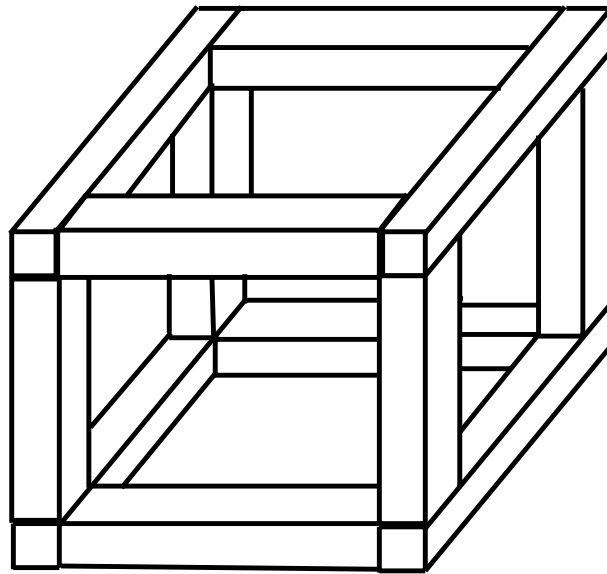
FIGURE 2-6: a 2 by 2 by 2 substrate volume discretization to demonstrate how the filaments, in Figure 2-5, are connected.
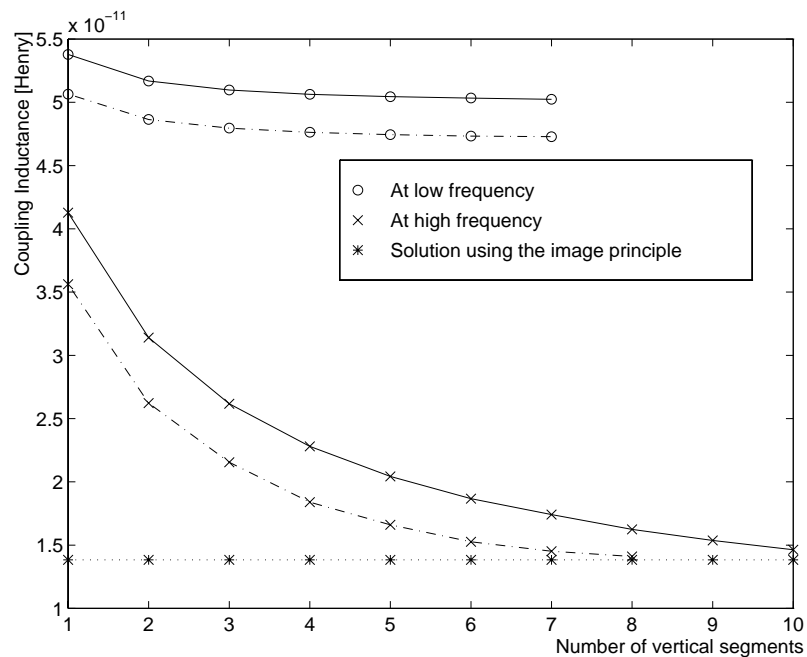
FIGURE 2-7: Convergence of the coupling inductance with discretization refinement. Solid line represents 30μ substrate thickness, and the dashed line represents 20μ substrate thickness.
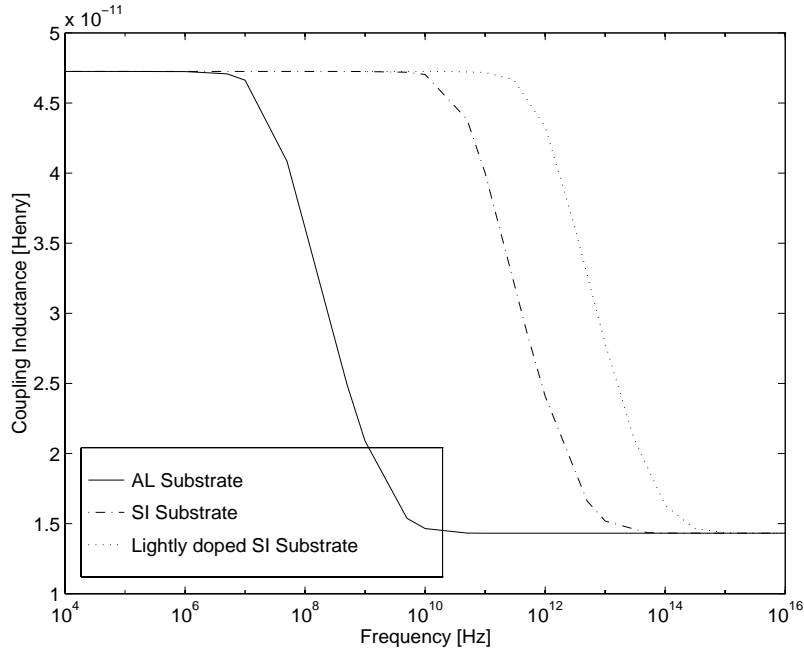
FIGURE 2-8: Inductance as a function of frequency for both an aluminum and semiconductor substrate. Substrate thickness is 20μ.

between them.

In Figure 2-7, the coupling inductance as a function of volume discretization is plotted for both very high and very low frequency. As is also shown in Figure 2-7, the formula based on the two-loop model accurately predicts the high frequency coupling inductance. For this comparison, the loop height z in equation (2.1) was set to twice the distance to the substrate, based on the method of images approach [35].

The modified Fasthenry program was also used to compute the coupling inductance as a function of frequency, for both realistic and idealized substrate conductivities. The results are plotted in Figure 2-8. Note that the results in Figure 2-8 clearly indicates that with a semiconductor substrate ($10^{19}cm^{-3}$ doped silicon), and assuming operating frequencies below 20 gigahertz, it is the low-frequency-limit inductance, *not* the high-frequency-limit inductance, that is most important for predicting on-chip inductive coupling. Figure 2-8 also shows that the transition from low-frequency-limit inductance to high-frequency-limit inductance occurs at much higher frequency than 20 gigahertz for lighter doped silicon substrates. For instance, it occurs at 100 gigahertz for a $10^{17}cm^{-3}$
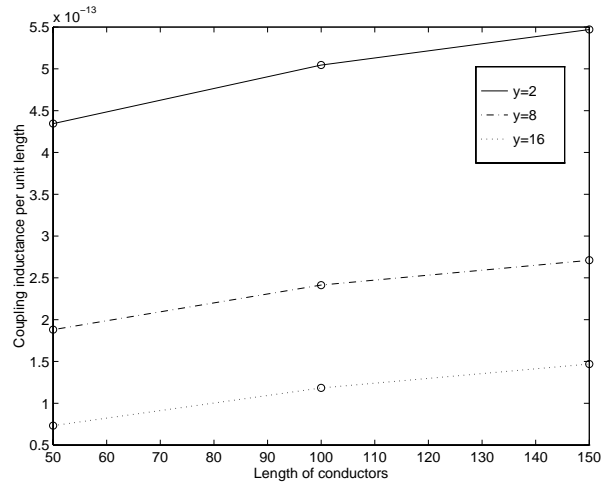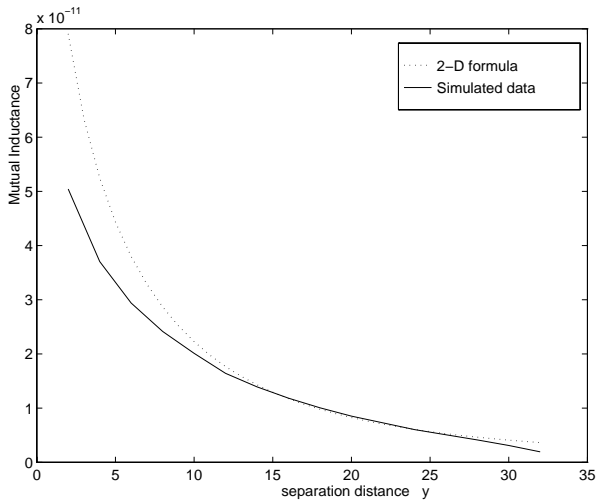
FIGURE 2-9: Comparison of the coupling inductance predicted by the two loop model with a "best-fit" loop height of 14.3μ, and the simulated coupling inductance as a function of separation distance.

FIGURE 2-10: Inductance per unit length as a function of conductor length, for different separation distances.
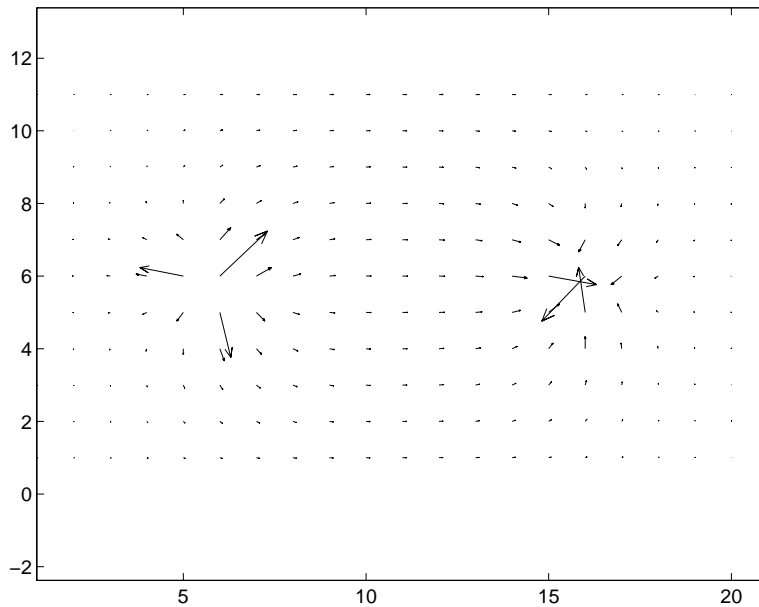
FIGURE 2-11: Typical low-frequency substrate surface current distribution.

doped silicon substrate.

2.5   Limitations of the Standard Approach

The two-loop model is inadequate for modeling the low-frequency-limit inductance. In Figure 2-9, it is shown that even by selecting a modified loop width, z, in the two-loop model of Figure 2-3, the model does not accurately predict parallel line inductive coupling over a range of conductor separations. Note that a "best-fit" loop height of 14.3μ was used for the comparison but the conductors are only 1μ above the ground plane.

The simple model fails primarily because the low-frequency coupling inductance over a substrate ground plane is more three-dimensional in nature than can be modeled by a loop. This is demonstrated clearly in Figure 2-10, where the plots of inductance per unit length show a significant change with conductor length. This three-dimensional behavior is due primarily to the current spreading from the contact points through the substrate, as shown in Figure 2-11.

2.6   Effect of Coupling Inductance on Signal Integrity

In order to simulate the effect of the coupling inductance on circuit crosstalk, we ran our program on some examples. Consider 16 parallel 1000μ long data lines, where 15 of them are switching simultaneously, as shown in Figure 2-12. The capacitance was calculated using the capacitance simulator, Fastcap [32]. The devices used were 0.5μ device technology. Step input signals with a rise time of 0.15 nsec were used to simulate the clock.

As shown in Figure 2-13, a voltage glitch of more than 1 volt appears at the end of the unswitched bus lines. Another example is a bus crossing structure consisting of two levels of four conductors, as shown in Figure 2-14. The bus structure produces a voltage glitch of 0.6 volts at the end of one line when the other 7 conductors are simultaneously
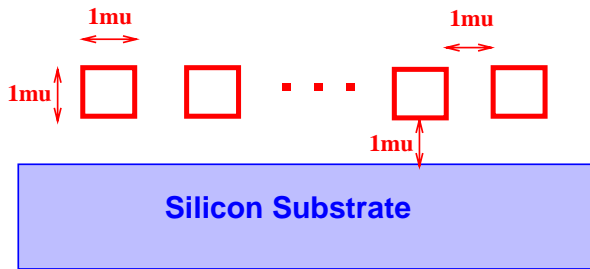
FIGURE 2-12: 16 Bit Data Bus, running over 30μthick silicon substrate. Length of each line is 1000μ.
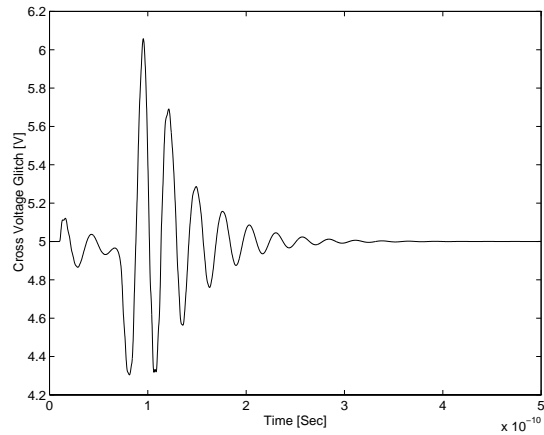
FIGURE 2-13: Cross-coupled voltage glitch appears on the unswitched line due to the simultaneous switching of the other bits on the 16 bit data bus example.
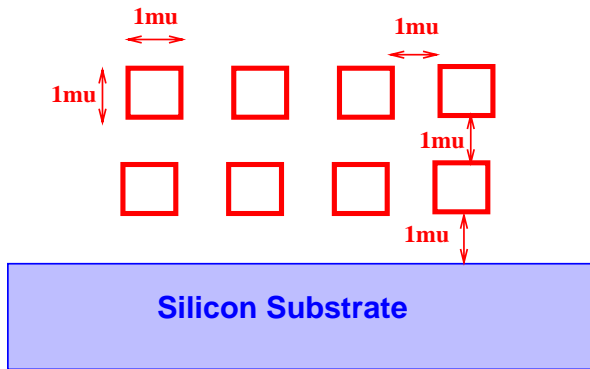
FIGURE 2-14: Two levels of conductors, each level consists of 4 conductors Length of each line is 1000μ.
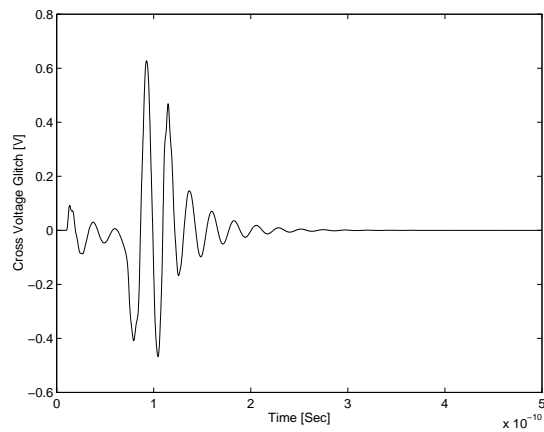
FIGURE 2-15: Cross-coupled voltage glitch appears on the unswitched line due to the simultaneous switching of the other lines on the 2 by 4 bus example.

switching, as shown in Figure 2-15.

2.7   Reducing Interconnect Coupling Inductance

It is possible to reduce the coupling inductance by using aluminum interconnect current return paths, rather than substrate return paths, as shown in Figure 2-16. Figure 2-17 shows that for a separation $y = 3\mu$, the coupling inductance when using an interconnect return path is less than that of using a substrate return path as long as the distance to the return path, x, less than 400μ. However, in order to get a significant reduction in the coupling inductance, the return paths must be very close to the original conductor, For instance, to get a 5 times reduction in the coupling inductance, x should be less than 3μ.

In order to verify this method of the coupling inductance reduction, and show its effect on circuit cross-talk, an example of 8 parallel 1000μ data lines is used. Figure 2-18 shows the cross voltage glitch that results on the unswitched line when other bits are simultaneously switching. It shows that the voltage glitch get reduced 3 times when every other line is grounded. This reduction in the coupling inductance cross voltage glitch was expected in the previous section, since the return path is close to the original conductor. The cost of this cross-talk reduction is that twice the number of lines has been used.

2.8   Analyzing Shielding Effects

Figure 2-19 shows that when grounding every third line, the cross voltage glitch is reduced by a factor of 1.5. The Figure also shows that the voltage glitch get reduced by an insignificant factor of 1.2 when grounding every fourth line. Consequently, the farther the ground line from the original conductor, the more insignificant the reduction of the cross-talk is. These simulation results proved that, coupling inductance can be reduced if aluminum interconnect current return paths is used rather than substrate return paths,

36
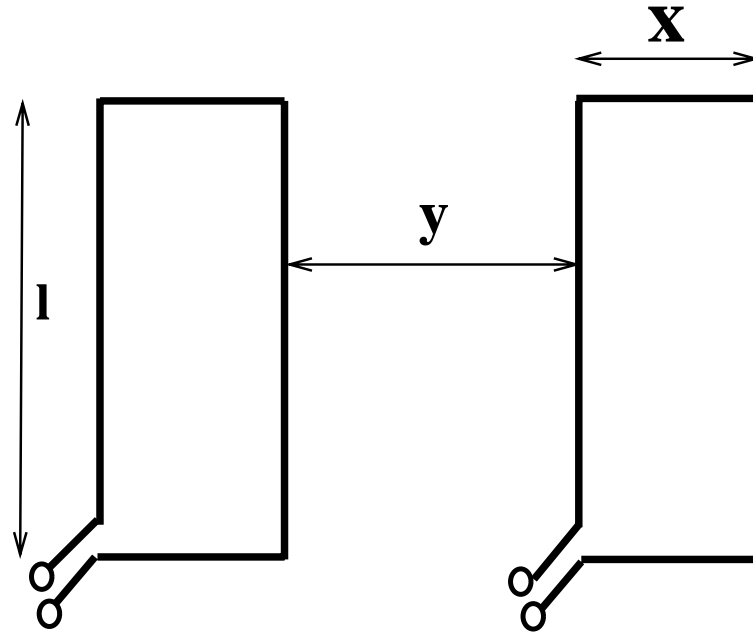
FIGURE 2-16: Returning path is through conductor rather than through the substrate. $l = 100\mu$, $y = 3\mu$.
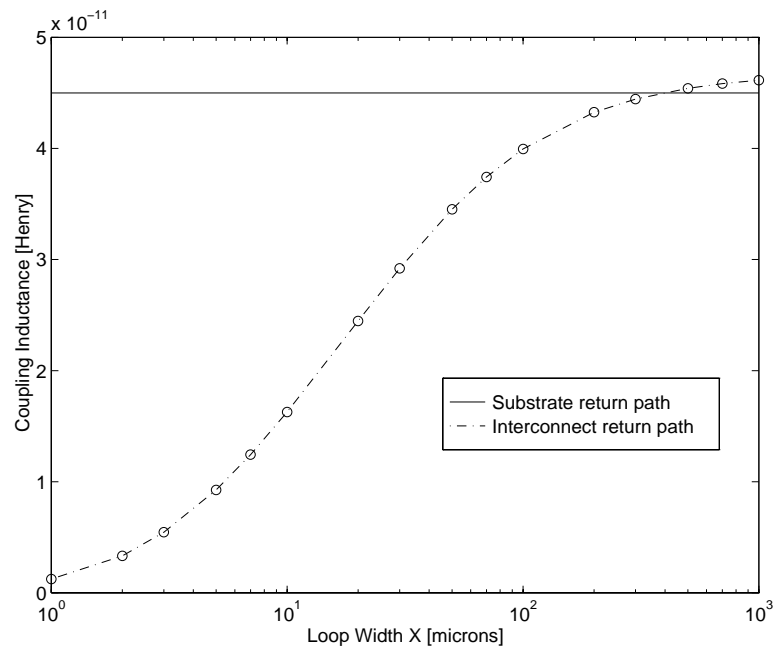
FIGURE 2-17: Coupling Inductance for both cases of conductor return path and substrate return path.
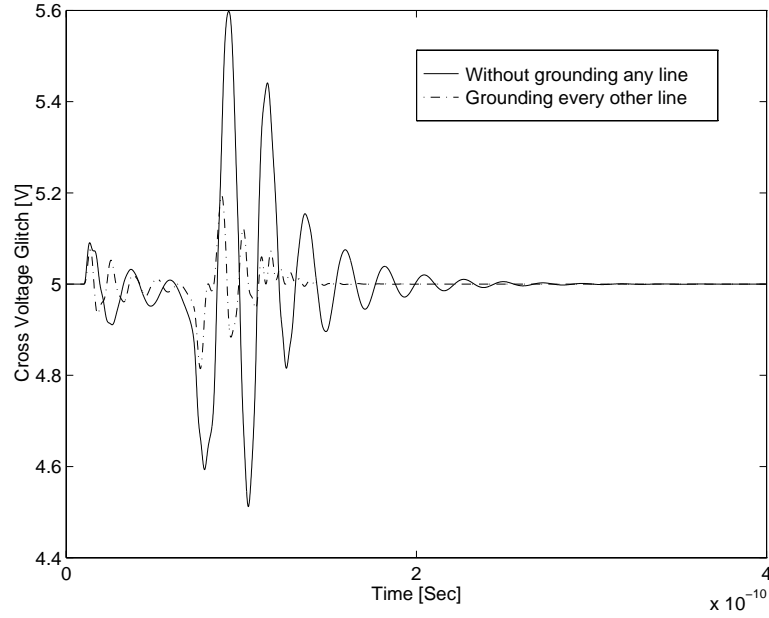
FIGURE 2-18: Cross-coupled voltage glitch appears on the unswitched line due to the simultaneous switching of the other bits on the 8 bit data bus. It also shows the voltage glitch that produce when grounding every other line.
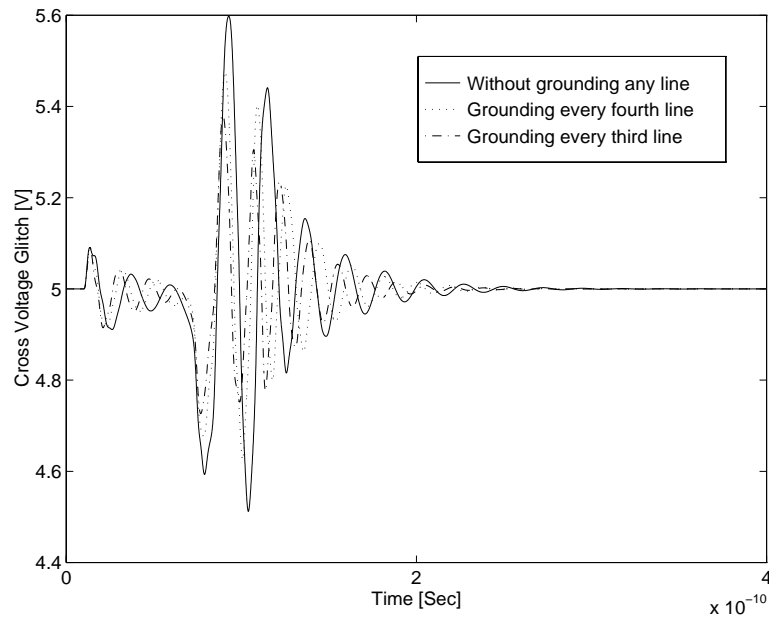
FIGURE 2-19: Cross-coupled voltage glitch appears on the unswitched line due to the simultaneous switching of the other bits on the 8 bit data bus. It also shows the voltage glitch that produce when grounding every third or fourth line.

and that these return paths have to be very close to the original conductors. The cost for this coupling inductance reduction technique is that more ground lines will be used.

Minimizing Interconnect Self Inductance

3.1   Motivation

Because magnetic effects have a much longer spatial range than electrostatic effects, an interconnect line with large inductance will be sensitive to distant variations in interconnect topology. This long range sensitivity makes it difficult to balance delays in nets like clock trees, so for such nets self inductance must be minimized. Figure 3-1 shows a schematic of a typical coplanar H clock tree, where the self inductance is needed to be minimized. A cross sectional view of that clock tree is shown in Figure 3-2.

Because consecutive metal layers are usually orthogonal to each other, there is no inductive coupling between lines in consecutive layers. Thus, the problem of minimizing the inductance of the structure in Figure 3-2 is reduced to minimizing the inductance of the structure in Figure 3-3.

3.2   Two-Dimensional Self Inductance

We used a typical clock structure to explore some methods for minimizing the self inductance, and therefore reduce the clock delay, and clock skew. The structure used is a clock signal line sandwiched between ground return lines, as indicated in Figure 3-3.
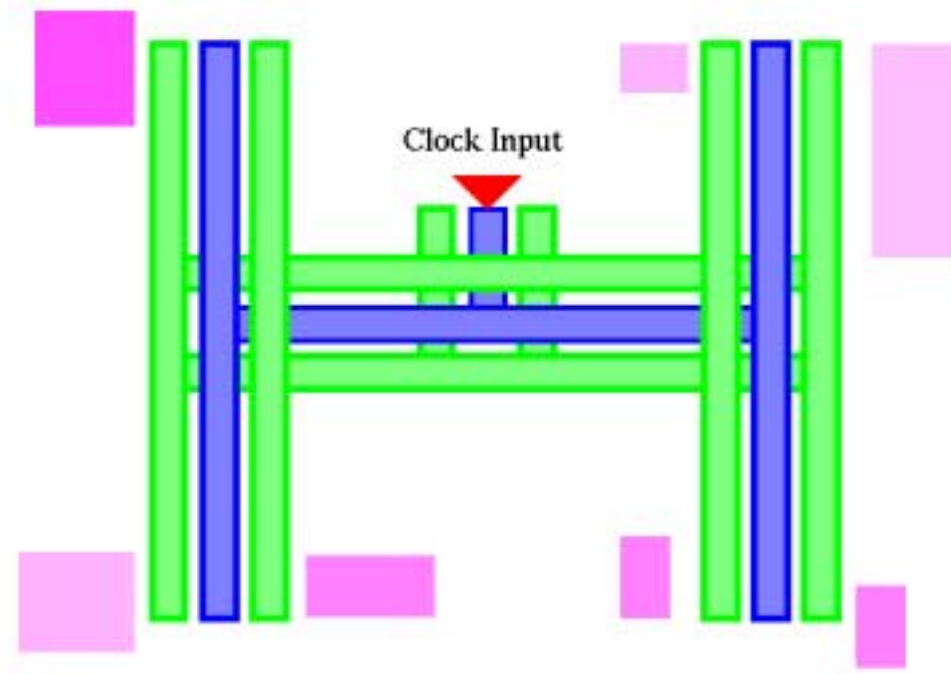
FIGURE 3-1: Schematic of a typical H Clock tree
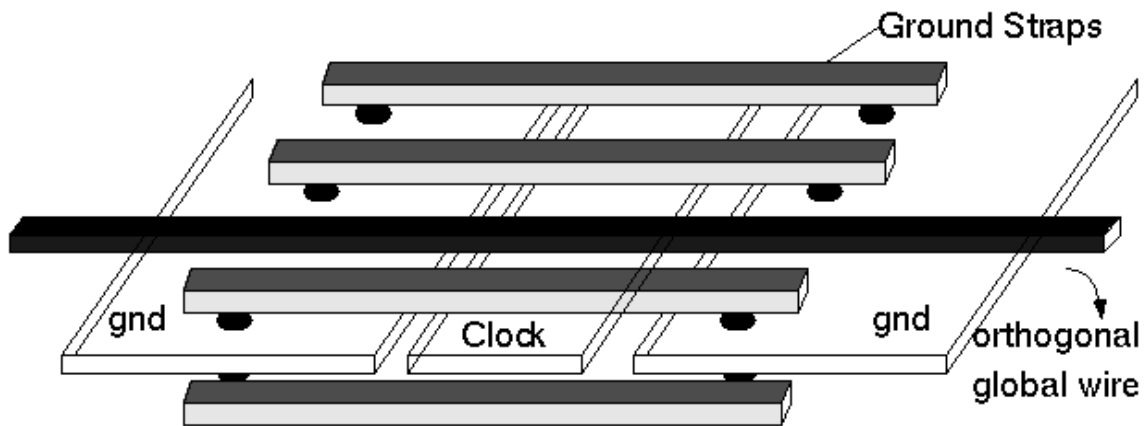
FIGURE 3-2: Cross section in a coplanar clock tree

We used a two-dimensional field solver for the inductance and fixed the width of the clock signal line, W1, and the width of the ground return lines, W2, to 1μ. As expected, we found that two-dimensional inductance increases as the separation distance between the clock signal line and the ground lines, S, increases, as shown in Figure 3-4. Thus, in order to minimize the inductance, the separation distance between the clock signal line and the ground return lines, S, should be as small as possible. The two-dimensional
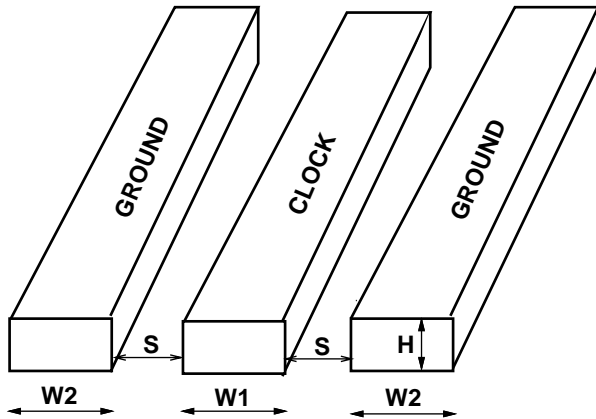
FIGURE 3-3: Coplanar Interconnect Clock Example
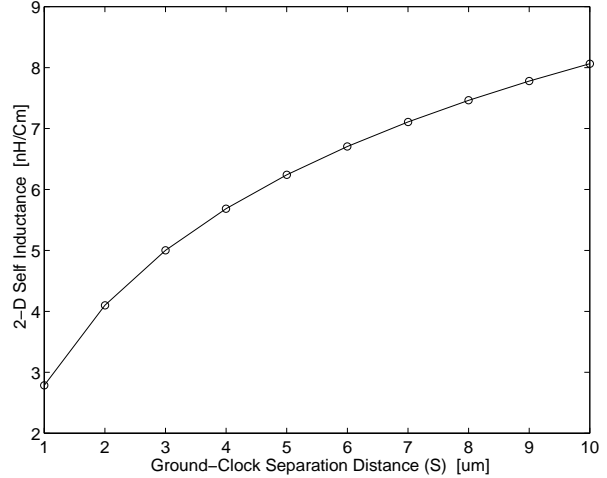
FIGURE 3-4: Variation of two-dimensional self inductance with the separation distance between the signal and the ground lines.

inductance is calculated assuming high frequency meaning that fields exist only outside the conductors.

3.3   Three-Dimensional Self Inductance

It is often presumed, as was in the previous section, that near gigahertz clock rates imply that on-chip inductive effects can be analyzed by determining high frequency limit current distributions. In order to verify this assumption and get the specific frequency at which the conductors behave as perfect conductors, we did a frequency sweep on the inductance of the clock structure using the 3-D field solver FastHenry [4]. FastHenry employs multipole-accelerated Method-of-Moments techniques [5,6].

In Figure 3-5, we show the frequency dependence of the self inductance of the structure shown in Figure 3-3, where $W1 = W2 = S = 1\mu$. Note that the 2-D self inductance computed in the previous section is, as expected, the high frequency limit of the 3-D self inductance computed by FastHenry. Figure 3-5 also shows that for frequencies less than twenty-five gigahertz, it is the low-frequency self inductance not the high frequency self inductance that determines inductive effects. The corner frequency for self-inductance is determined by the skin effect. The thinner the conductor is, the higher the corner
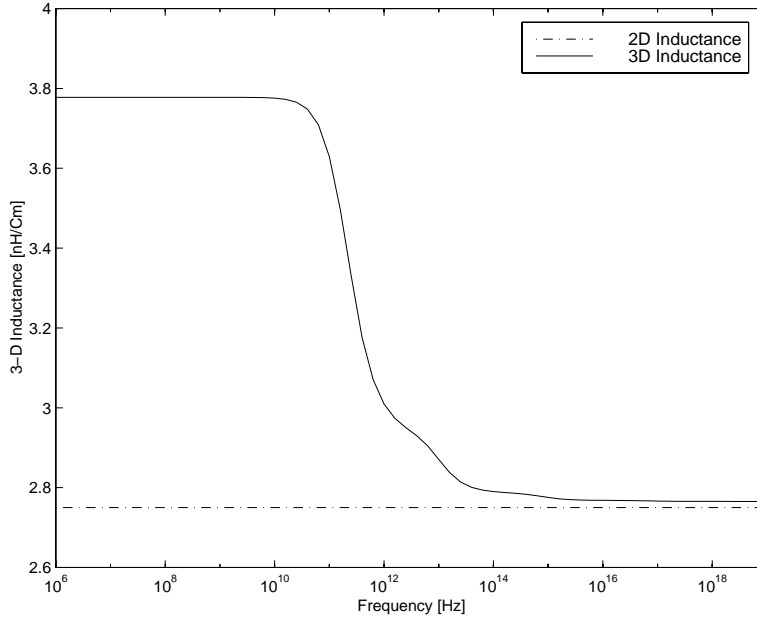
FIGURE 3-5: Three-dimensional self inductance frequency dependence for the clock structure in Figure (coplan) . $W1 = W2 = S = 1\mu$.

frequency. Note that, in new technologies, conductor widths are getting to be much smaller than 1μ, and therefore the corner frequency is getting higher. This guarantees that the self inductance of interest is the low-frequency one.

Figure 3-6 shows the frequency dependence of the resistance for the same structure. It shows that structure resistance has the DC resistance value for frequencies below the corner frequency and as frequency increases beyond the corner frequency, the resistance increases due to the skin effect.

3.4   Reducing Self Inductance

3.4.1   Optimizing Dimensions of Same Clock Structure

In order to determine the optimum structure that minimizes the self inductance of the clock, we started by keeping the same structure in Figure 3-3 and trying to optimize its dimensions to reach minimum inductance. As shown in Figure 3-7,

The inductance decreases as the width of the clock signal line, W1, increases, till it
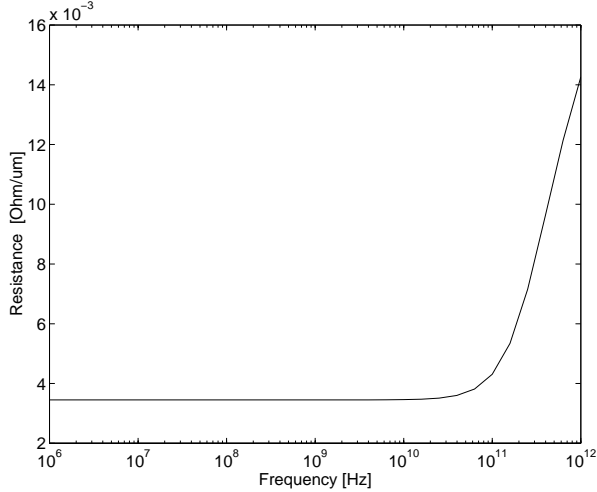
FIGURE 3-6: Resistance frequency dependence for the clock structure in Figure (coplan). $W1 = W2 = S = 1\mu$.
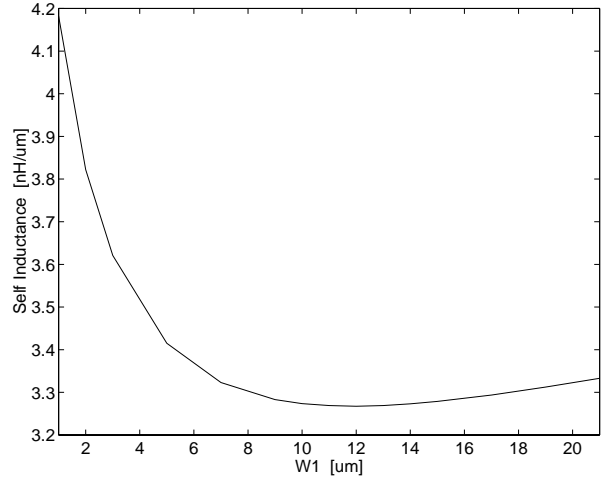
FIGURE 3-7: Variation of self inductance with W1 for the clock structure in Figure (coplan). $W2 = 3\mu, S = 1\mu$.

reaches a minimum value at $W1 = 12\mu$. After this minimum the inductance increases as W1 increases. The resistance of the clock is always decreasing as W1 is increasing as shown in Figure 3-8. This curve is not a linear function of W1 due to the constant resistance of the ground return lines, W2. The component of the total resistance from W1 continues to fall off linearly, but the total value saturates at the ground return value. The 3-D capacitance solver FastCap [7] was used to measure the capacitance of the structure. In the capacitance model, conductors in upper and lower metal layers were represented, as they influence the capacitance of the clock structure. Note that without including the surrounding conductors in the upper and lower metal layers, changes in capacitance between the conductors would be grossly over-estimated. Figure 3-9 shows that the capacitance is increasing linearly with W1.

Consider the two following structures, the first has $W1 = 3\mu$, $W2 = 3\mu$, and $S = 1\mu$, and the second has $W1 = 12\mu$, $W2 = 3\mu$, and $S = 1\mu$. The second structure has been optimized for minimum inductance given fixed $W2 = 3\mu$, its inductance is 10% less than the first structure. This 10% reduction in the inductance was achieved by using 2.3 times the original space, and 120% increase in the capacitance as shown in Figure 3-9.

Therefore, techniques for widening the clock to lower resistance, has little impact on
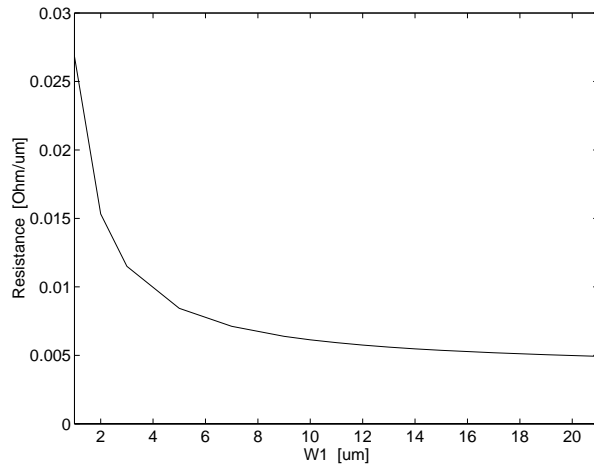
FIGURE 3-8: Variation of resistance with W1 for the clock structure in Figure (coplan). $W2 = 3\mu$, $S = 1\mu$.
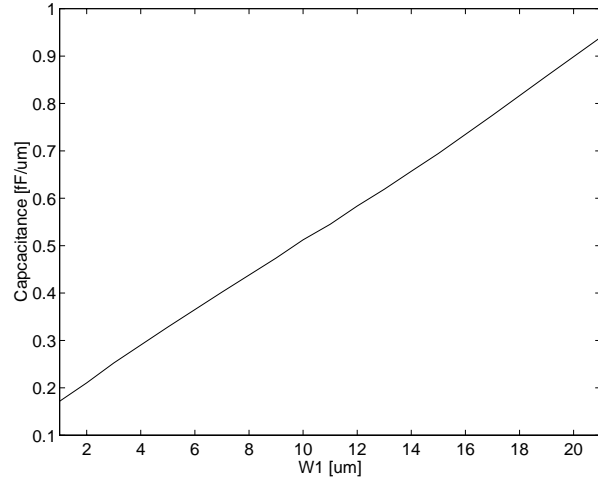
FIGURE 3-9: Variation of Capacitance with W1 for the clock structure in Figure (coplan). $W2 = 3\mu$, $S = 1\mu$.
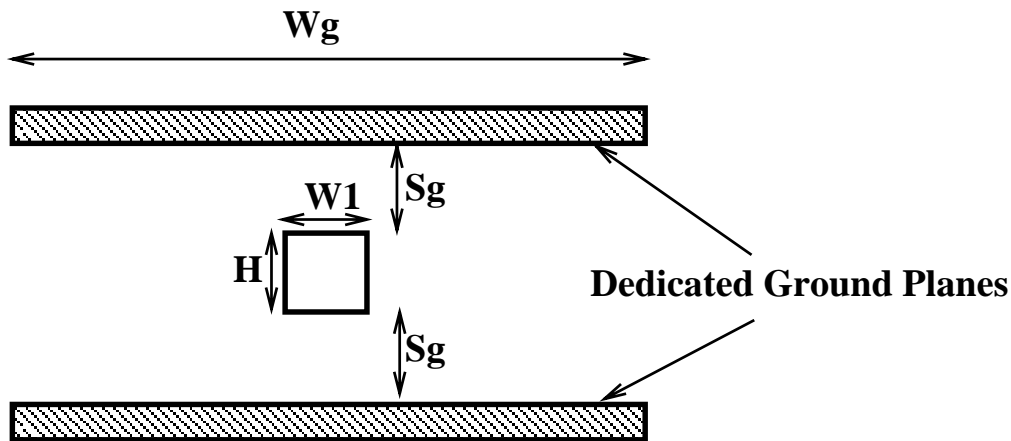
FIGURE 3-10: Using dedicated ground planes as return paths for the clock signal.

the inductance. On the contrary, it might increase the capacitance significantly.

3.4.2   Using Dedicated Ground Plane Techniques

We also investigated using dedicated ground planes as return paths for the clock signal, as shown in Figure 3-10.

Figure 3-11 shows the low frequency self inductance as a function of the ground plane width, Wg. Figure 3-11 also shows that, at around $Wg = 4\mu$, the inductance has a minimum value. After that minimum value, the low frequency self inductance increases

46
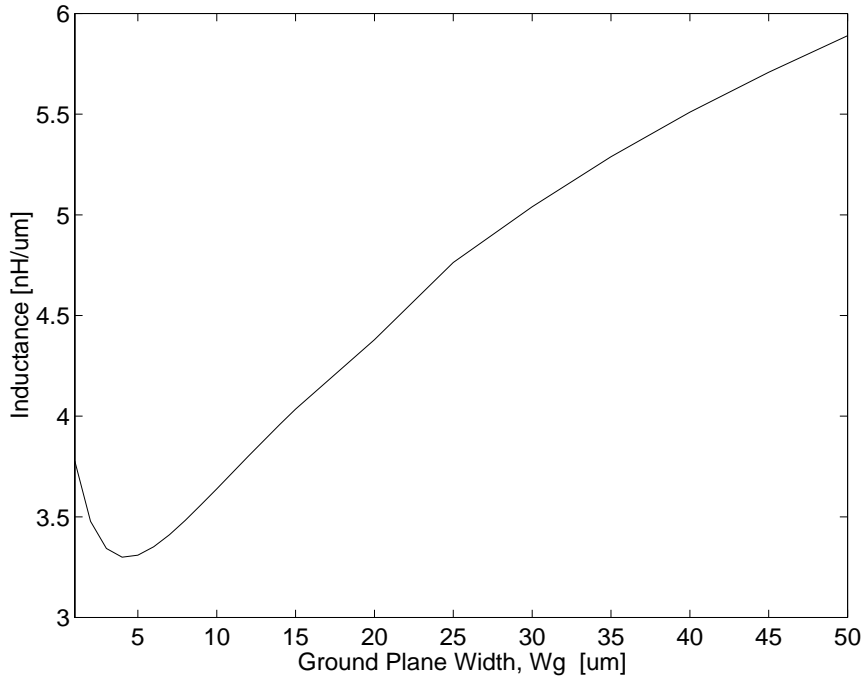
FIGURE 3-11: Self inductance for the dedicated ground plane structure. $W1 = H = Sg = 1\mu$.

monotonically as Wg increases. The current, at low frequency, is uniformly distributed on the ground plane, therefore, big current loops are formed when Wg is large. This increases the inductance. Figure 3-12 compares the self inductance frequency response of the dedicated ground planes case, with $W1 = H = Sg = 1\mu, Wg = 100\mu$, and the two ground traces case, same as in Figure 3-5. Figure 3-12 also shows the frequency response when having both the ground traces and the ground planes as return paths. As shown in Figure 3-12, using only guard traces technique has the smallest inductance unless the frequency of interest exceed several GHz. Above that frequency, dedicated ground planes have somewhat lower inductance, but since most of the energy in the signal is below several GHz, the use of dedicated ground planes is ineffective in reducing the self inductance.

3.4.3 Using Interdigitated Techniques

As space is always a limiting factor for chip designs, it would be best if the inductance can be significantly reduced with only a limited increase of the total space allocated for
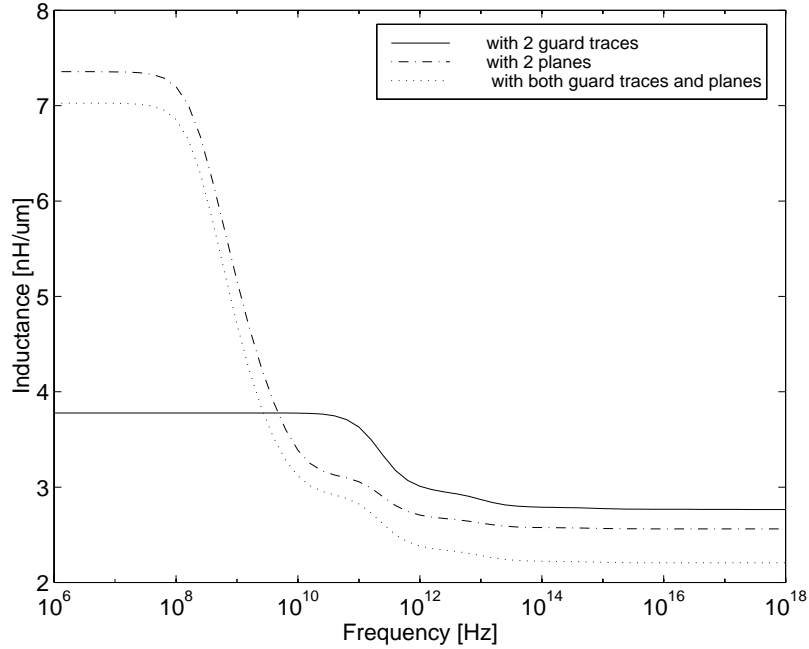
FIGURE 3-12: Self inductance Frequency response for the dedicated ground plane case shown in Figure (dedicatG), $W1 = H = Sg = 1\mu, Wg = 100\mu$, the guard traces case, as in Figure (3d) , and both ground traces and ground plane case.
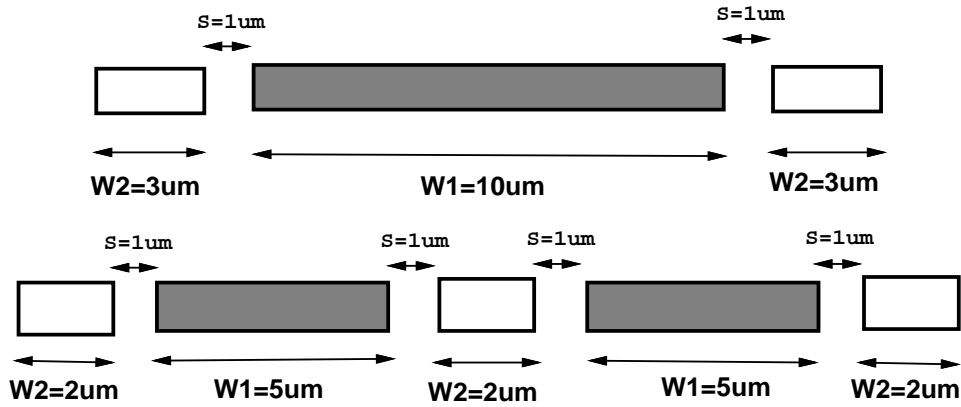
FIGURE 3-13: Interdigitated clock structure, using 5 lines instead of 3 lines. Total structure width has been increased from 18μ to 20μ.

the clock structure. In order to achieve that, one might think of distributing the clock signal on many lines, and doing the same for the ground return lines. As shown in Figure 3-13,

The 10μ signal line has been divided into two 5μ lines. Similarly, the two 3μ ground returns have been exchanged by three 2μ ground returns. This design resulted in no

48

change in resistance, a 27% increase in capacitance, a 43% decrease in inductance, and only an 11% increase in area. The inductance is not reduced by 50%, as might be expected, due to the non-opposing mutual inductances.

We tried different interdigitated structures, keeping the total structure width increase to less than 20%. Table 3-1 shows that a significant reduction of the self inductance of the clock can be achieved increasing the number interconnect lines in the clock structure. Table 3-2 shows the relative change in the RLC performance, for all structures.

N	W1	W2	Wt	$R[m\Omega/\mu]$	$L[nH/Cm]$	$C[fF/\mu]$
3	10μ	3μ	18μ	R1=6.1	L1=3.273	C1=.5124
5	5μ	1μ	17μ	9.9	1.927	.6449
5	5μ	2μ	20μ	6.1	1.869	.6483
7	3μ	1μ	19μ	8.3	1.336	.7345
9	2μ	1μ	21μ	7.5	1.027	.8215
11	1μ	1μ	21μ	8.4	0.850	.8478

Table 3-1: Variation of the resistance, inductance and capacitance of the clock structure with the number of interconnect lines in the structure, N, and the total width of the clock structure, Wt. All lines are separated from adjacent lines by 1um.

N	W1	W2	Wt	R/R1	L/L1	C/C1
3	10μ	3μ	18μ	1.00	1.00	1.00
5	5μ	1μ	17μ	1.62	0.59	1.26
5	5μ	2μ	20μ	1.00	0.57	1.27
7	3μ	1μ	19μ	1.36	0.41	1.43
9	2μ	1μ	21μ	1.23	0.31	1.60
11	1μ	1μ	21μ	1.38	0.26	1.66

Table 3-2: Relative Variation of the resistance, inductance and capacitance of the clock structure with the number of interconnect lines in the structure, N, and the total width of the clock structure, Wt. All lines are separated from adjacent lines by 1um.

The resistance or the maximum space allowed for the clock, whichever is more critical in the design, determines the exact width for each line. As shown in Table 3-1, about the same reduction percentage in the inductance, can be achieved with two different 5 line structures. However, the five line structure with the 17μ wide clock structure has

62% more resistance than the 20μ wide clock structure. Table 3-2 also shows that the inductance can be reduced as low as 3.9 times by having the clock structure composed of 11 lines, where ground and signal lines are alternatively placed. This significant reduction in the inductance can be achieved with an insignificant increase in the total clock structure width, and clock resistance, and a modest increase in the capacitance.

Part II

Inductance Extraction for Structures that Contain Permeable Materials

There have been many methods to solve for the magnetostatic field in presence of linear magnetic materials. These methods yield the magnetic field by solving for the double scalar potential $\phi - \psi$ [36, 37, 38, 39, 40, 41, 42], the magnetization vector M [43], the fictitious current on the surface of the permeable material [44, 45] or the reduced scalar potential [46, 47, 48, 49].

The double scalar potential method uses two different formulations for the magnetic field depending on whether the evaluation point is inside or outside the permeable material. The method gives good accuracy but it solves for two scalar potential quantities, the total potential outside the permeable material, ψ, and the reduced potential inside the permeable material, ϕ . Both the magnetization vector method and the fictitious surface current have the disadvantage that they solve for vector quantities. This has the same effect as solving for three scalar components. The reduced scalar potential associated with the induced magnetic field is used in the whole region. The method solves for only one scalar potential, ϕ, but the method suffers poor accuracy when calculating fields inside highly permeable materials. This poor accuracy is caused by numerical cancellation errors resulting from subtracting two small quantities of the same order.

In this part, we develop a fast algorithm for efficient extraction of the frequency dependant inductance of structures with magnetic materials. The magnetic material considered consists of constant magnetic permeability, implying magnetic linearity of the problem. Moreover, eddy and displacement currents are ignored under the magnetquasistatic assumption.

In Chapter 4, we start by deriving a formulation for the magnetic field using a fictitious surface magnetic charge on the permeable material interface [49]. The method has the advantage of introducing only one scalar quantity, which is the scalar surface magnetic charge. Consequently, minimum number of unknowns are generated. The method, however, is considered a reduced potential method, and therefore, it inherits the possibility of numerical cancellation errors when solving for fields inside the permeable material. This problem is completely avoided in our formulation, because it avoids computing fields quantities inside the permeable material.

The magnetic field expression, generated in section 4.1, is then substituted in the boundary condition equation that ensures the continuity of the normal flux density across the permeable material interface. This leads to an integral equation that relates the magnetic charges to the current in the conductors. In section 4.2, an integral equation for the currents in the conductors is generated. The produced integral equation relates the currents in the conductors and the voltages across the conductors to the magnetic field, not the magnetic charges. After some mathematical manipulation, the term depending on the magnetic field in the current integral equation is replaced with another term that is dependant only on the magnetic charges. Thus, two coupled integral equations that relate currents, voltages, and surface magnetic charges are generated. Moreover, in section 4.3, we show that the coupled integral formulation leads to a linear system. Thus, for a given voltage, the linear system can be solved for the charges and the currents, and therefore, the frequency dependant inductance of the structure can be extracted.

In Chapter 5, we present how the individual integrals in the resulting linear system, from Chapter 4, can be calculated efficiently and accurately. In section 5.2, we compute the field due to the current sources. In section 5.3, we present two different methods to compute the integral that represents the effect of the magnetic charges on the current in the conductors, L_ρ. One of the two methods converts the integral into a line integral. This enables the automation of the integral computation process.

In section 5.4, we discuss efficient evaluation of the integral that represents the magnetic field due the magnetic charges. We then show that discretizing the boundary condition integral equation using a standard collocation method is inaccurate for materials with sharp geometric features and can be replaced by a qualocation method which is much more accurate and no more expensive than the collocation method.

In Chapter 6, we present computational experiments and demonstrate that the algorithm using the qualocation method more accurately predicts the magnetic field for the analytically solvable problem of a permeable ellipsoid in a uniform magnetic field.

We also compare the extracted inductance to published data for some practical examples. The algorithm predicted accurately the inductance of these examples. In section 6.2,

the resulting linear system is solved iteratively using a preconditioned GMRES method. The method is up to an order of magnitude faster than the standard direct method.

Integral Formulation for Structures with Permeable Materials

4.1   Equivalent Magnetic Problem

This section focuses on an integral equation formulation for modeling 3-D magneto-static field in presence of permeable materials.

Assume that regions that contain permeable materials are separated from current carrying conductors, as shown in Figure 4-1, as is the case in many magnetic problems. As illustrated in Figure 4-1, the volume of the magnetic problem consists of two parts. The first part is the volume of the magnetic material V_{core}, surrounded by a surface S_{core} and characterized by a permeability μ. The second part of the magnetic problem is the volume of the free space V_{air} and characterized by a free space permeability μ_0. The free space current sources are inside V_{air}.

The integral formulation is derived by assuming the magnetoquasistatic assumption, that the the frequencies of interest will be considered small enough such that the displacement current, $j\omega\epsilon\boldsymbol{E}$, can be neglected. Thus, Maxwell's equations using the magnetoquasistatic assumption are

$$\nabla \times \boldsymbol{E} \;\; = \;\; -jw\mu\boldsymbol{H} \tag{4.1}$$

$$\nabla \times \boldsymbol{H} \;\; = \;\; \boldsymbol{J} \tag{4.2}$$

$$\nabla \cdot (\epsilon\boldsymbol{E}) \;\; = \;\; \rho \tag{4.3}$$
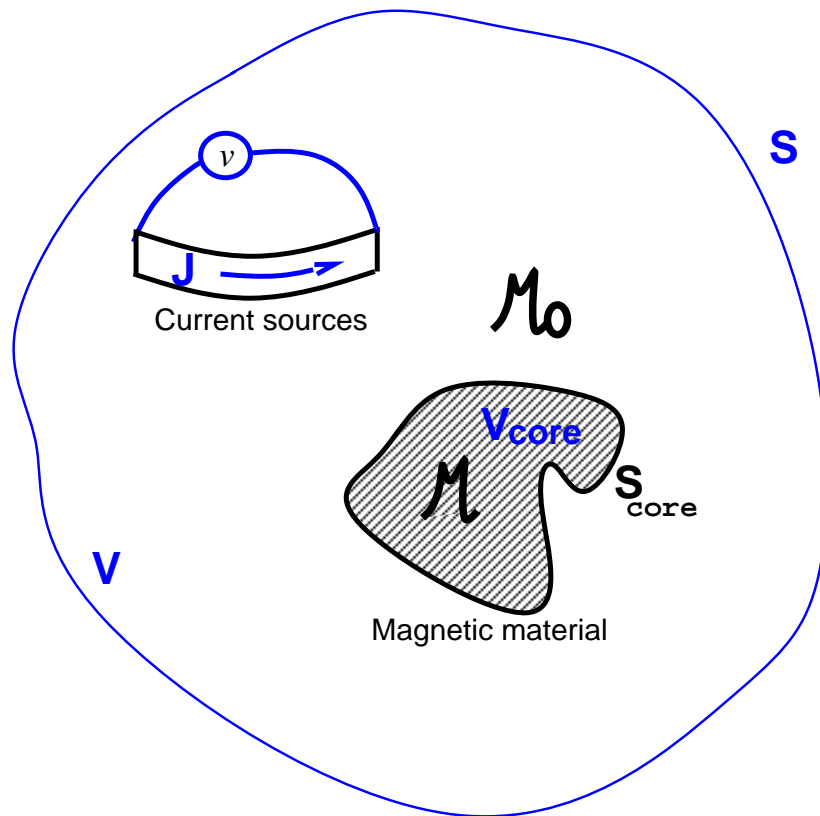
FIGURE 4-1: Current sources are outside the magnetic material

$$\nabla \cdot (\mu \boldsymbol{H}) = 0 \tag{4.4}$$

where ω is the angular frequency.

The magnetic field intensity at a point, H, can be separated into two parts, as follows:

$$H = H_c + H_m. \tag{4.5}$$

H_c is the free space field intensity that would exist if there were no permeable parts. H_c is directly the result of the current sources, so that

$$\nabla \times \boldsymbol{H}_c = J. \tag{4.6}$$

H_m is the magnetization component which results due to the presence of permeable regions. H_c is given by the Biot-Savart law [28, 50]:

$$H_c = \nabla \times \frac{1}{4\pi} \int_{V_{cond}} \frac{\boldsymbol{J}(r')}{|\boldsymbol{r} - \boldsymbol{r}'|} dv' = \frac{1}{4\pi} \int_{V_{cond}} \frac{\boldsymbol{J}(r') \times (r - r')}{|\boldsymbol{r} - \boldsymbol{r}'|^3} dv' \tag{4.7}$$

where V_{cond} is the volume of the conductors, r' is the source point vector and r is the field point vector.

From (4.2) and (4.6) we get,

$$\nabla \times \boldsymbol{H}_m = 0. \tag{4.8}$$

This implies,

$$H_m = -\nabla \Psi \tag{4.9}$$

where Ψ is the magnetic scalar potential.

Thus, the magnetic field intensity at a point, H is given by,

$$H(r) = \nabla \times \frac{1}{4\pi} \int_{V_{cond}} \frac{\boldsymbol{J}(r')}{|\boldsymbol{r} - \boldsymbol{r}'|} dv' - \nabla \Psi(r) \tag{4.10}$$

Taking the divergence of (4.10), and substituting from (4.4) results in ,

$$\nabla^2 (\Psi) = -\nabla \cdot \boldsymbol{H}(\boldsymbol{r}) \tag{4.11}$$

By expanding (4.4) we get ,

$$\mu(r)\nabla \cdot \boldsymbol{H}(\boldsymbol{r}) + \boldsymbol{H}(\boldsymbol{r}) \cdot \nabla \mu(r) = 0 \tag{4.12}$$

By substituting from (4.12) in (4.11),

$$\nabla^2(\Psi) = \frac{\boldsymbol{H}(\boldsymbol{r}) \cdot \nabla \mu(r)}{\mu(r)} \tag{4.13}$$

The right hand side of this (4.13) is zero everywhere, except on the surface of the magnetic, S_{core}. Hence, for simplicity, we can set the right hand side to $\rho_m(r)$, as in,

$$\nabla^2(\Psi) = -\rho_m(r) \tag{4.14}$$

where $\rho_m(r)$ is an equivalent fictitious magnetic charge density, since it is zero everywhere except on the magnetic material surface.

Equation (4.14) has the solution

$$\Psi(r) = \frac{1}{4\pi} \int_{S_{core}} \frac{\rho_m(r')}{|\boldsymbol{r} - \boldsymbol{r}'|} ds' \tag{4.15}$$

Thus, the magnetic field intensity at a point becomes,

$$H(r) = \frac{1}{4\pi} \int_{V_{cond}} \frac{\boldsymbol{J}(r') \times (r - r')}{|\boldsymbol{r} - \boldsymbol{r}'|^3} dv' - \frac{1}{4\pi} \nabla \int_{S_{core}} \frac{\rho_m(r')}{|\boldsymbol{r} - \boldsymbol{r}'|} ds' \tag{4.16}$$

and the magnetic flux density is

$$B(r) = \frac{\mu(r)}{4\pi} \int_{V_{cond}} \frac{\boldsymbol{J}(r') \times (r - r')}{|\boldsymbol{r} - \boldsymbol{r}'|^3} dv' - \frac{\mu(r)}{4\pi} \nabla \int_{S_{core}} \frac{\rho_m(r')}{|\boldsymbol{r} - \boldsymbol{r}'|} ds' \tag{4.17}$$

4.1.1 Boundary Condition Equation

The Boundary condition at a point p on the interface is

$$\boldsymbol{B}_{core}.n(p) = \boldsymbol{B}_{air}.n(p) \tag{4.18}$$

where $n(p)$ is the unit vector perpendicular to S_{core} at p. The left hand side of this equation becomes

$$\boldsymbol{B}_{core}.n(p) = \frac{\mu_0 \mu_r}{4\pi} \int_{V_{cond}} \nabla \frac{1}{R} \times \boldsymbol{J}(r') \cdot n(p) dv' - \frac{\mu_0 \mu_r}{4\pi} \nabla \int_{S_{core}} \frac{\rho_m(r')}{R} ds' \cdot n(p) \tag{4.19}$$

where $R = |p - r'|$. The gradient can be brought inside the surface integral since it operates on p, whereas the integral operates on r'. For the same reason, $\rho_m(r')$ can

60

be brought outside the gradient. The integrand is zero except when $p = r'$. Then a singularity appears, which evaluates to $2\pi\rho_m(p)$. Hence equation (4.19) becomes

$$\boldsymbol{B}_{core}.n(p) = \frac{\mu_0\mu_r}{4\pi}\left[\int_{V_{cond}}\nabla\frac{1}{R}\times\boldsymbol{J}(r')\cdot n(p)dv' + 2\pi\rho_m(p)\right]$$
$$-\frac{\mu_0\mu_r}{4\pi}\left[\int_{S_{core-p}}\rho_m(r')n(p)\cdot\nabla\frac{1}{R}ds'\right] \qquad (4.20)$$

Similarly for the air region

$$\boldsymbol{B}_{air}.n(p) = \frac{\mu_0}{4\pi}\left[\int_{V_{cond}}\nabla\frac{1}{R}\times\boldsymbol{J}(r')\cdot n(p)dv' - 2\pi\rho_m(p)\right]$$
$$-\frac{\mu_0\mu_r}{4\pi}\left[\int_{S_{core-p}}\rho_m(r')n(p)\cdot\nabla\frac{1}{R}ds'\right] \qquad (4.21)$$

Substituting equations (4.20) and (4.21) into (4.18) gives the integral equation valid at the interface

$$2\pi\frac{\mu_r + 1}{\mu_r - 1}\rho_m(p) = \int_{V_{cond}}\nabla\frac{1}{R}\times\boldsymbol{J}(r')\cdot n(p)dv' - \int_{S_{core-p}}\rho_m(r')n(p)\cdot\nabla\frac{1}{R}ds' \qquad (4.22)$$

The analysis in this section showed that linear magnetic materials can be modeled as magnetic surface charges distributed on the material interfaces, as shown in Figure 4-2. These charges should satisfy equation (4.22).

4.1.2   Discretization of Magnetic Charges

The magnetic material interface can be divided into triangular or quadrilateral panels, on which charge density is assumed constant, as shown in Figure 4-2. The approximation to the charge density distribution can then be written as

$$\rho_m(p) \approx \sum_{j=1}^{n} q_j w_j(p) \qquad (4.23)$$

where q_j is the charge on panel j, and $w_j(r)$ is the weighting function which has a value of zero outside panel j, and $1/A_j$ on panel j where A_j is the area of the panel j.

61

Original Problem   **Equivalent Problem**   **Discretized Equivalent Problem**
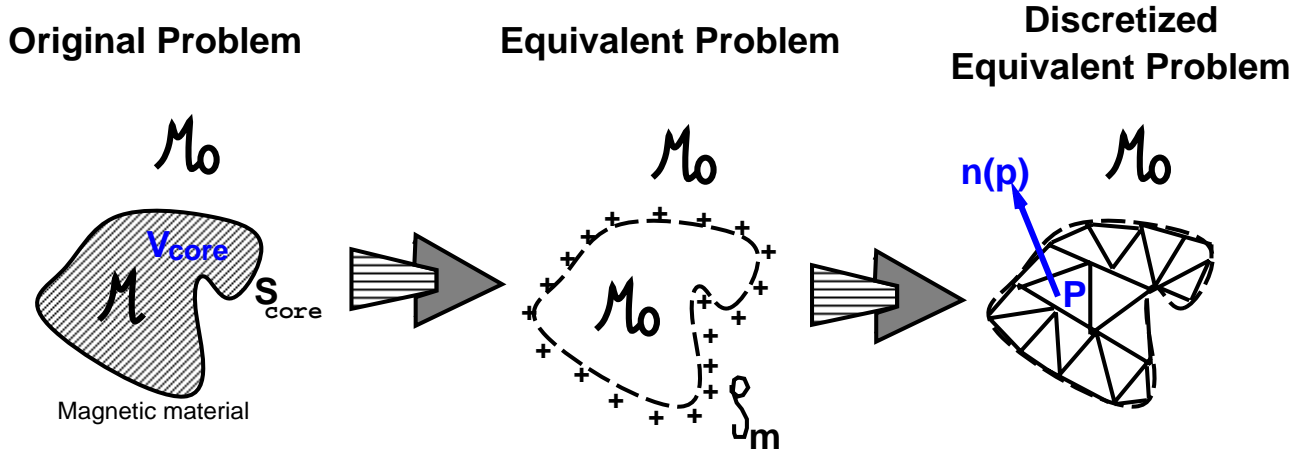
FIGURE 4-2: Linear magnetic material can be represented with an equivalent free space problem with magnetic surface charges distributed on the magnetic material interfaces. The interface is discretized into panels on which charge is assumed constant

Substituting the charge density expansion (4.23) into (4.22), yields

$$2\pi \frac{\mu_r + 1}{\mu_r - 1} \frac{q_j}{A_j} + \sum_{j=1}^{n} \frac{q_j}{A_j} \int_{panel\ j} n(p) \cdot \nabla \frac{1}{R} ds' = -\int_{V_{cond}} \nabla \frac{1}{R} \times \boldsymbol{J}(r') \cdot n(p) dv' \quad (4.24)$$

If the current density is known, a linear system can be formed as

$$AQ = C \quad (4.25)$$

where Q is the vector of the unknown panel charges,

$$C_i = \int_{V_{cond}} \nabla \frac{1}{R} \times \boldsymbol{J}(r') \cdot n(p) dv', \quad (4.26)$$

$$A_{ij} = \frac{1}{A_j} \int_{panel\ j} n(p) \cdot \nabla \frac{1}{R} ds' \quad i \neq j, \quad (4.27)$$

and

$$A_{ii} = 2\pi \frac{\mu_r + 1}{\mu_r - 1} \frac{q_j}{A_j} \quad (4.28)$$

Unfortunately, only for few cases, the current distribution is known a priori, such as at very low frequency, where the current distribution is uniform across the cross section of the conductors. Thus, for a general frequency of operation, the current density is needed to to be solved for, and therefore, another equation for the current needs to be derived.

4.2 Current Integral Formulation

In this section we get an integral formulation for the current. By assuming the magnetoquasistatic assumption, the current density, J, within the conductors is,

$$\boldsymbol{J} = \sigma \boldsymbol{E} \tag{4.29}$$

where σ is the conductivity.

Taking the divergence of (4.2) results in the current conservation equation,

$$\nabla \cdot \boldsymbol{J} = 0. \tag{4.30}$$

Because of the zero divergence of the magnetic flux density $\boldsymbol{B}$ in (4.4) , the magnetic flux density vector can be defined as,

$$\boldsymbol{B} = \mu \boldsymbol{H} = \nabla \times \boldsymbol{A} \tag{4.31}$$

where $\boldsymbol{A}$ is the vector potential.

Substituting from (4.31) in (4.1) produces,

$$\nabla \times (\boldsymbol{E} + jw\boldsymbol{A}) = 0. \tag{4.32}$$

This implies that there exists a scalar function, Φ, such that

$$-\nabla\Phi = \boldsymbol{E} + jw\boldsymbol{A} \tag{4.33}$$

where Φ will be called the scalar potential.

We require one final relation to relate the vector potential, $\boldsymbol{A}$ to the current density, $\boldsymbol{J}$. By taking the curl of both sides of use of (4.31) and choosing the Coulomb gauge,

$$\nabla \cdot \boldsymbol{A} = 0. \tag{4.34}$$

we get,

$$-\nabla^2 A = \mu \nabla \times H + \nabla \mu \times H \tag{4.35}$$

and thus,

$$\boldsymbol{A}(r) = \frac{1}{4\pi} \int_{V_{cond}} \frac{\mu(r')\boldsymbol{J}(r')}{|\boldsymbol{r} - \boldsymbol{r}'|} dv' + \frac{1}{4\pi} \int_{S_{core}} \frac{\nabla\mu(r') \times H(r')}{|\boldsymbol{r} - \boldsymbol{r}'|} ds' \tag{4.36}$$

where V_{cond} is the volume of all conductors, S_{core} is the surface of the magnetic material, and $\mu(r')$ in the first integral is the permeability of the space containing the conductors, which is equal to μ_0. Note that the second integral in the previous equation is a surface integral, because $\nabla \mu(r')$ is zero everywhere except on the surface of the magnetic material.

Substituting (4.36) and (4.29), into (4.33) yields the following integral equation:

$$\frac{\boldsymbol{J}(r)}{\sigma} + \frac{jw\mu_0}{4\pi} \int_{V_{cond}} \frac{\boldsymbol{J}(r')}{|\boldsymbol{r} - \boldsymbol{r}'|} dv' + \frac{jw}{4\pi} \int_{S_{core}} \frac{\nabla\mu(r') \times H(r')}{|\boldsymbol{r} - \boldsymbol{r}'|} ds' = -\nabla\Phi(r). \quad (4.37)$$

4.2.1 Discretization of the Current Equation

By using the magnetoquasistatic assumption, the current within a long thin conductor can be assumed to flow parallel to its surface. The conductor can be divided into piecewise straight segments. In order to capture skin and proximity effects properly, each of these segments can be divided into a bundle of parallel filaments of rectangular cross-section inside which the current is assumed to flow along the length of the filament, as shown in Figure 4-3. The mesh currents, shown in Figure 4-3, are the currents around each mesh [51] in the network. They satisfy

$$M^t I_m = I_b, \quad (4.38)$$

where $I_m \in C^m$ is the vector of mesh currents, I_b is the vector of branch currents except for the source branches, and $M \in R^{m \times b}$ is the mesh matrix, where $m = n * b - n + 1$ is the number of meshes, b is the number of segments, and n is the number of filaments per segment.

We use mesh currents as basis for the current density. It will be shown in the next chapter that, because of this selection of the basis function, the current integral equation can transformed to be function of the scalar magnetic charges rather than the vector magnetic field.

Using this basis function, the current distribution can be approximated as

$$\boldsymbol{J}(r) \approx \sum_{i=1}^{m} I_i w_i(r) \mathbf{l_i} \quad (4.39)$$

Current sources

Divide into Segments

Ibranch1

Ibranch3

Filament

IM1   Mesh1

IM2   Mesh2

v_t $\;\begin{array}{c}+\\-\end{array}$

Ibranch2

Ibranch4

IM3   Mesh3
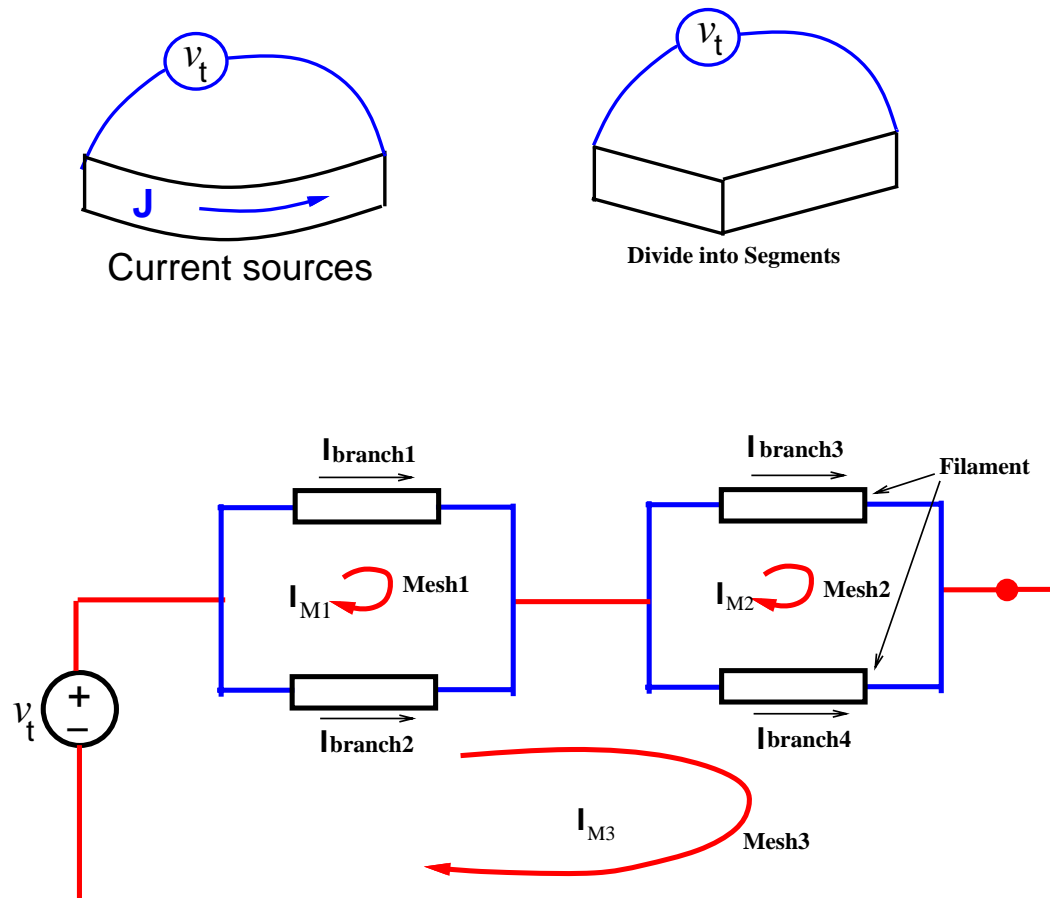
FIGURE 4-3: (a) One conductor, (b) divided into piecewise-straight segments, (c) discretized into filaments. Notice how the mesh currents are related to the branch currents

where I_i is the current in mesh i, $\mathbf{l_i}$ is a unit vector along the length of the mesh and $w_i(r)$ is the weighting function which has a value of zero outside mesh i, and $1/a_i$ inside, where a_i is the cross sectional area of the filaments in mesh i.

Following the method of moments [52], a system of m equations can be generated by taking the inner product of each of the weighting functions with the vector integral equation (4.37). Then multiplying both sides with a_i gives,

$$\sum_{j=1}^{m} \sum_{f=1}^{\#filaments\ in\ mesh\ j} \left(\frac{1}{\sigma a_f} \int_{L_i} \mathbf{l_i} \cdot \mathbf{l_f}\, dL \right) I_j$$

$$+ j\omega \sum_{j=1}^{m} \sum_{f=1}^{\#filaments\ in\ mesh\ j} \left(\frac{\mu_0}{4\pi a_f} \int_{L_i} \int_{V'_f} \frac{\mathbf{l_i} \cdot \mathbf{l_f}}{|\boldsymbol{r} - \boldsymbol{r}'|} dV'\, dL \right) I_j$$

$$+ \frac{jw}{4\pi} \int_{L_i} \int_{S_{core}} \frac{\nabla \mu(r') \times H(r')}{|\boldsymbol{r} - \boldsymbol{r}'|} ds'\, dL = \int_{L_i} \left(-\nabla \Phi(r) \right) dL = -V_{m_i} \qquad (4.40)$$

where σ is the conductivity, L_i is the lengths of mesh i, V'_f is the volume of filament f in mesh j, and V_{m_i} is the voltage across mesh i. Note that the right hand side of (4.40) results from integrating $\nabla \Phi$ along the length of the ith mesh.

4.2.2 Relating Current Formulation to Magnetic Charges

The third term in (4.40) is depending on the magnetic field, H. This term need to be transfered into other terms that are directly dependant on the currents, J and the magnetic charge density, ρ_m. We start by applying Stokes theorem [53] to the third term in (4.40)

$$\frac{jw}{4\pi} \int_{L_i} \int_{S_{core}} \frac{\nabla \mu(r') \times H(r')}{|\boldsymbol{r} - \boldsymbol{r}'|} ds'\, dL = \frac{jw}{4\pi} \int_{S_i} \nabla \times \int_{S_{core}} \frac{\nabla \mu(r') \times H(r')}{|\boldsymbol{r} - \boldsymbol{r}'|} ds'\, dS \quad (4.41)$$

where S_i is the surface area of the current mesh i. The shape of S_i is arbitrary, as shown in Figure 4-4.

Substituting from (4.36) into (4.31) will result in an expression of the magnetic field

66
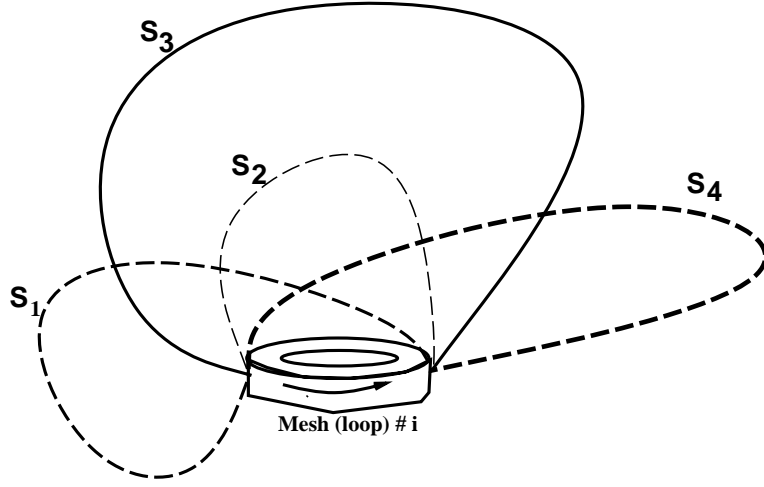
FIGURE 4-4: S_1, S_2, S_3 *and* S_4 could be possible surfaces for S_i. Stokes theorem transfers the line integral across a mesh i into a surface integral over the surface S_i. Note that the shape of S_i is arbitrary

density,

$$B(r) = \frac{1}{4\pi} \int_{V_{cond}} \mu_0 \frac{\boldsymbol{J}(r') \times (r - r')}{|\boldsymbol{r} - \boldsymbol{r}'|^3} dv' + \frac{1}{4\pi} \nabla \times \int_{S_{core}} \frac{\nabla \mu(r') \times H(r')}{|\boldsymbol{r} - \boldsymbol{r}'|} ds' \qquad (4.42)$$

By equating the two expressions for the magnetic flux density in (4.17) and (4.42), we get

$$\nabla \times \int_{S_{core}} \frac{\nabla \mu(r') \times H(r')}{|\boldsymbol{r} - \boldsymbol{r}'|} ds' = (\mu(r) - \mu_0) \int_{V_{cond}} \frac{\boldsymbol{J}(r') \times (r - r')}{|\boldsymbol{r} - \boldsymbol{r}'|^3} dv'$$

$$- \mu(r) \int_{S_{core}} \rho_m(r') \nabla \frac{1}{|\boldsymbol{r} - \boldsymbol{r}'|} ds' \qquad (4.43)$$

By substituting from (4.43) into (4.41), the third term in (4.40) becomes,

$$\frac{jw}{4\pi} \int_{L_i} \int_{S_{core}} \frac{\nabla \mu(r') \times H(r')}{|\boldsymbol{r} - \boldsymbol{r}'|} ds' dL = \frac{jw}{4\pi} \int_{S_i} (\mu(r) - \mu_0) \int_{V_{cond}} \frac{\boldsymbol{J}(r') \times (r - r')}{|\boldsymbol{r} - \boldsymbol{r}'|^3} dv' dS$$

$$- \frac{jw}{4\pi} \int_{S_i} \mu(r) \int_{S_{core}} \rho_m(r') \nabla \frac{1}{|\boldsymbol{r} - \boldsymbol{r}'|} ds' \cdot dS \qquad (4.44)$$

If the surface S_i in (4.44) is chosen to penetrate the magnetic material, the two surface integrals in Equation (4.44) are almost equal but with opposite signs, which may result in numerical cancellation errors.

Taking into consideration that S_i can be of any shape, as long as it encircles current mesh i, one can usually find a surface S_i that does not to penetrate the magnetic material. Note that most of structures that contain permeable materials contain an air gap. Therefore, if such a surface S_i is chosen, $\mu(r)$ in (4.44) will be equal to μ_0, and consequently, the second integral in (4.44) vanishes. Thus, we get

$$\frac{jw}{4\pi} \int_{L_i} \int_{S_{core}} \frac{\nabla \mu(r') \times H(r')}{|\boldsymbol{r} - \boldsymbol{r'}|} ds'dL = -\frac{jw\mu_0}{4\pi} \int_{S_i} \int_{S_{core}} \rho_m(r')\nabla \frac{1}{|\boldsymbol{r} - \boldsymbol{r'}|} ds' \cdot dS \quad (4.45)$$

where S_i is a surface that encloses mesh i and does not penetrate the magnetic material.

By interchanging the two double surface integrals in (4.45), and then substituting in (4.40), we get

$$\sum_{j=1}^{m} \sum_{f=1}^{\#filaments\ in\ mesh\ j} \left(\frac{1}{\sigma a_f} \int_{L_i} \mathbf{l_i} \cdot \mathbf{l_f}\, dL \right) I_j$$

$$+ j\omega \sum_{j=1}^{m} \sum_{f=1}^{\#filaments\ in\ mesh\ j} \left(\frac{\mu_0}{4\pi a_f} \int_{L_i} \int_{V_f'} \frac{\mathbf{l_i} \cdot \mathbf{l_f}}{|\boldsymbol{r} - \boldsymbol{r'}|} dV'\, dL \right) I_j$$

$$- \frac{jw\mu_0}{4\pi} \int_{S_{core}} \rho_m(r')ds' \int_{S_i} \nabla \frac{1}{|\boldsymbol{r} - \boldsymbol{r'}|} \cdot dS = V_{m_i} \qquad (4.46)$$

By discretizing the magnetic surface charge density on the magnetic material interface, $\rho_m(r')$, the same way as in (4.23), the current integral equation becomes

$$\sum_{j=1}^{m} \sum_{f=1}^{\#filaments\ in\ mesh\ j} \left(\frac{1}{\sigma a_f} \int_{L_i} \mathbf{l_i} \cdot \mathbf{l_f}\, dL \right) I_j$$

$$+ j\omega \sum_{j=1}^{m} \sum_{f=1}^{\#filaments\ in\ mesh\ j} \left(\frac{\mu_0}{4\pi a_f} \int_{L_i} \int_{V_f'} \frac{\mathbf{l_i} \cdot \mathbf{l_f}}{|\boldsymbol{r} - \boldsymbol{r'}|} dV'\, dL \right) I_j$$

$$- \frac{jw\mu_0}{4\pi} \sum_{k=1}^{n} q_k \int_{S_i} \nabla \frac{1}{|\boldsymbol{r} - \boldsymbol{r'}|} \cdot dS = V_{m_i} \qquad (4.47)$$

where q_k is the charge on panel k on the magnetic material interface,

4.3   Coupled Integral Formulation

By discretizing the current in (4.22) using the mesh current basis in (4.39) and assuming long thin conductors so the volume integral in (4.22) is approximated as a line integral, we get

$$
2\pi \frac{\mu_r + 1}{\mu_r - 1} \frac{q_k}{A_k} + \sum_{k=1}^{n} \frac{q_k}{A_k} \int_{panel\ k} n(p) \cdot \nabla \frac{1}{|\boldsymbol{r} - \boldsymbol{r'}|} ds'
$$
$$
= -\sum_{i=1}^{m} \frac{I_i}{a_i} \int_{L_{mesh_i}} \nabla \frac{1}{|\boldsymbol{r} - \boldsymbol{r'}|} \times \mathbf{l_i} \cdot n(p) dL' \tag{4.48}
$$

Equations (4.47) and (4.48) form a coupled integral equation system to solve for the mesh currents, I_j, and the magnetic surface charges on the magnetic material interface, q_k. The two coupled integral equations can be summarized in the matrix form as

$$
\begin{bmatrix} R(\omega) + j\omega L_J(\omega) & j\omega L_\rho(\omega) \\ H n_J & (H n_\rho - I) \end{bmatrix} \begin{bmatrix} \overline{I}_M \\ \overline{q}_k \end{bmatrix} = \begin{bmatrix} V \\ 0 \end{bmatrix} \tag{4.49}
$$

where $\overline{I}_M \in C^m$ is the vector of m mesh currents, and $\overline{q}_k \in C^k$ is the vector of n charge panels,

In order to extract the inductance of a set of conductors, the admittance matrix Y_t needs to be calculated. The admittance matrix can be calculated using

$$
Y_t(\omega) V_t(\omega) = I_t(\omega), \tag{4.50}
$$

where $I_t, V_t \in C^k$ are vectors of the terminal current and voltage respectively [51]. To evaluate the ith column of the admittance matrix, Y_t , we solve (4.49) with a vector V whose only nonzero entry corresponds to V_t, and then extract the entries of I_M associated with the source branches. For example, for the one conductor circuit shown in Figure 4-3, we solve (4.49) with a vector V whose only nonzero entry is the third element and equal to one. The admittance of the circuit is the third element in the solution vector, I_M.

In the following chapter, we discuss how the individual elements in (4.49) can be calculated efficiently and accurately.

Efficient Evaluation of the Integrals in the Magnetic Integral Formulation

In the previous chapter, we derived the magnetic coupled integral formulation (4.49). In this chapter, we discuss how the individual integrals in resulting linear matrix system (4.49) can be calculated efficiently and accurately.

5.1 Evaluation of sub-matrices R and L_J

This section briefly describes the calculation of the sub-matrices R and L_J in the linear system (4.49).

L_J and R are the $m \times m$ loop inductance matrix, and loop resistance matrix and loop inductance, respectively. A general element in the sub-matrix L is given by

$$Lij = \sum_{f=1}^{\#filaments\ in\ mesh\ j} \frac{j\omega\mu_0}{4\pi a_f} \int_{L_i} \int_{V'_f} \frac{\mathbf{l_i} \cdot \mathbf{l_f}}{|\boldsymbol{r} - \boldsymbol{r}'|} dV' dL \tag{5.1}$$

where σ is the conductivity, V'_f is the volume of filament f in mesh j, $\mathbf{l_i}$ is the unit length along the length of the ith mesh, a_f is the cross sectional area of filament f, $\mathbf{l_f}$ is the unit length along the length of the filament, f, and L_i is the length of the ith mesh.

A general element in the sub-matrix R is given by

$$R_{ij} = \sum_{f=1}^{\#filaments\ in\ mesh\ j} \frac{1}{\sigma a_f} \int_{L_i} \mathbf{l_i} \cdot \mathbf{l_f}\, dL \qquad (5.2)$$

The mesh matrices can be computed directly from (5.1) and (5.2). As a matter of fact, these sub-matrices are related to the partial inductance model [54, 55, 56] via the following equations

$$L = ML_pM^t$$

$$R = MR_pM^t \qquad (5.3)$$

where M is the sparse mesh matrix, L_p is the $N_f \times N_f$ partial inductance matrix, with N_f is the total number of filaments,

$$L_{p_{fk}} = \left[\frac{j\omega\mu_0}{4\pi a_f a_k} \int_{V_f} \int_{V_k'} \frac{\mathbf{l_f} \cdot \mathbf{l_k}}{|\boldsymbol{r} - \boldsymbol{r}'|} dV'\, dV \right], \qquad (5.4)$$

R_p is the $N_f \times N_f$ diagonal matrix of filament DC resistances, and

$$R_{p_{ff}} = \frac{l_f}{\sigma a_f} \qquad (5.5)$$

where a_f is the cross sectional area of filament i, and l_f is the length of filament f, V_f is the volume of filament f, and V_k is the volume of filament k.

The elements in (5.4) can be computed using analytical formulas for partial mutual inductance and partial self inductance of rectangular filaments [57].

5.2   Evaluation of Magnetic Field due to Currents

In this section, we describe an efficient way to evaluate the elements of the sub-matrix Hn_J in the linear system (4.49). An element $[Hn_J]_{ki}$ is the magnetic field due to current mesh i, at point r_k, dotted with the unit normal to panel k, n_k, as shown in Figure 5-1. $[Hn_J]_{ki}$ is the sum of line integrals over all the filaments that constitute mesh i, as in
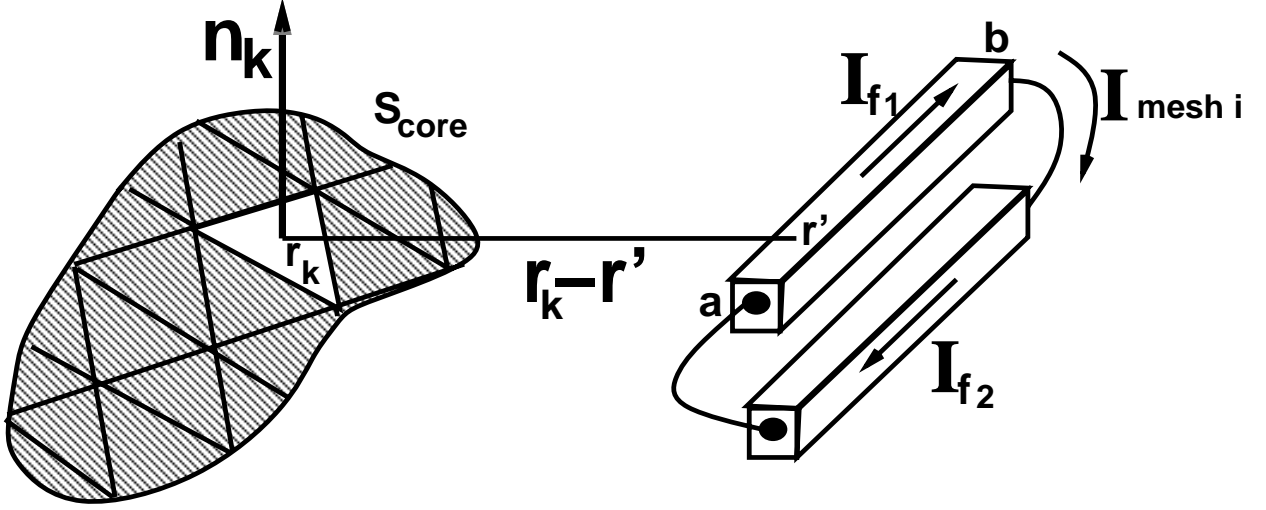
FIGURE 5-1: Evaluating $[Hn_J]_{ki}$, the magnetic field due to current mesh i, at point r_k, dotted with the unit normal to panel k, n_k.

$$[Hn_J]_{ki} = \sum_{f=1}^{\#filaments\ in\ mesh\ i} \int_{L_{filament\ f}} \nabla \frac{1}{|r_k - r'|} \times \mathbf{l_f} \ \cdot \ n_k dl'$$

$$= \sum_{f=1}^{\#filaments\ in\ mesh\ i} G_{kf} \qquad (5.6)$$

where $\mathbf{l_f}$ is the unit vector along the length of filament f.

Each element, G_{kf}, in the summation in (5.6) can be calculated by transforming each filament into the panel coordinates. In the new coordinate system, the current filament f is chosen to be aligned on the new x axis and the panel center lies in the new x-y plane, as shown in Figure 5-2.

Following this transformation, we get an analytical expression for G_{kf} as in,

$$G_{kf} = \frac{1}{L_3} \left(\frac{L_1 - L_2}{\sqrt{(L_1 - L_2)^2 + L_3^2}} + \frac{L_2}{\sqrt{L_2^2 + L_3^2}} \right) * n_k'(3) \qquad (5.7)$$

where $n_k'(3)$ is the z component of the transformed n_k to the new coordinate system, as shown in Figure 5-2. Thus by using (5.6) and (5.7), we get an analytical formula for the elements of Hn_J in the linear system (4.49).

73
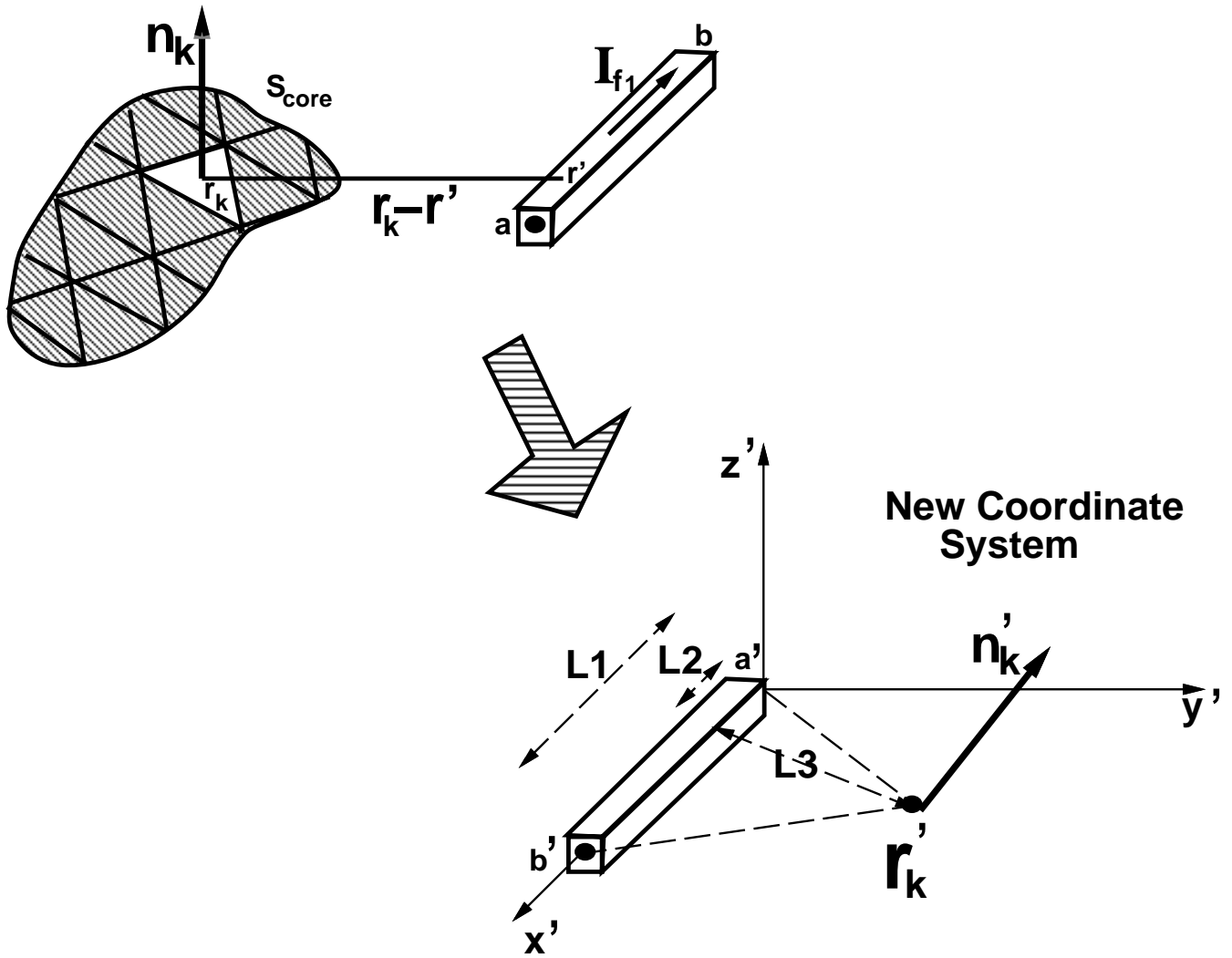
FIGURE 5-2: Evaluating $[Hn_J]_{ki}$, using an analytical expression which is produced by transforming to a new coordinate system.

5.3 Evaluation of Effect of Magnetic Charge on Mesh Currents, L_ρ

In this section, we describe an efficient way to evaluate the elements of the sub-matrix L_ρ in the linear system (4.49). An element $[L_\rho]_{ki}$ is the effect of the magnetic charge of panel k of on mesh current i is given by,

$$[L_\rho]_{ki} = -\frac{j\omega\mu_0}{4\pi} \int_{S_{mesh\ i}} \nabla\frac{1}{|r - r'|} \cdot n(r)dS \qquad (5.8)$$

where n(r) is the normal the surface of current mesh i at point r.

5.3.1 Evaluating $[L_\rho]_{ki}$ Using A Surface Integral

The integral in (5.8) comes from integrating 1/r over the surface of current loop i and evaluating the result at a point at the permeable material surface. Since the shape of the surface of the current loop is arbitrary. we can choose a surface like the tented one, shown in Figure 5-3. This tented surface is composed of triangles, and so $[L_\rho]_{ki}$ is given by:

$$[L_\rho]_{ki} = -\frac{j\omega\mu_0}{4\pi} \sum_{\triangle} \int_{S_\triangle} \nabla_r\frac{1}{|\ r - r'\ |} \cdot n(\triangle)dS_\triangle \qquad (5.9)$$

where $S_\triangle$ is a triangle on the current loop surface, and $n(\triangle)$ is the normal to triangle on the current loop (mesh) surface. The integral inside the summation in (5.9) is the potential due to a dipole charge distribution on a triangles. This potential can be evaluated analytically [58, 59].

5.3.2 Evaluating $[L_\rho]_{ki}$ Using A Line Integral

Although, the shape of the surface of the current loop is arbitrary, that surface should be selected such that it doesn't penetrate the magnetic material as discussed in subsection (4.2.2).

The current loop surface that doesn't penetrate the magnetic material can be very complicated, as in spiral inductor problems. Additionally, the process of selecting that
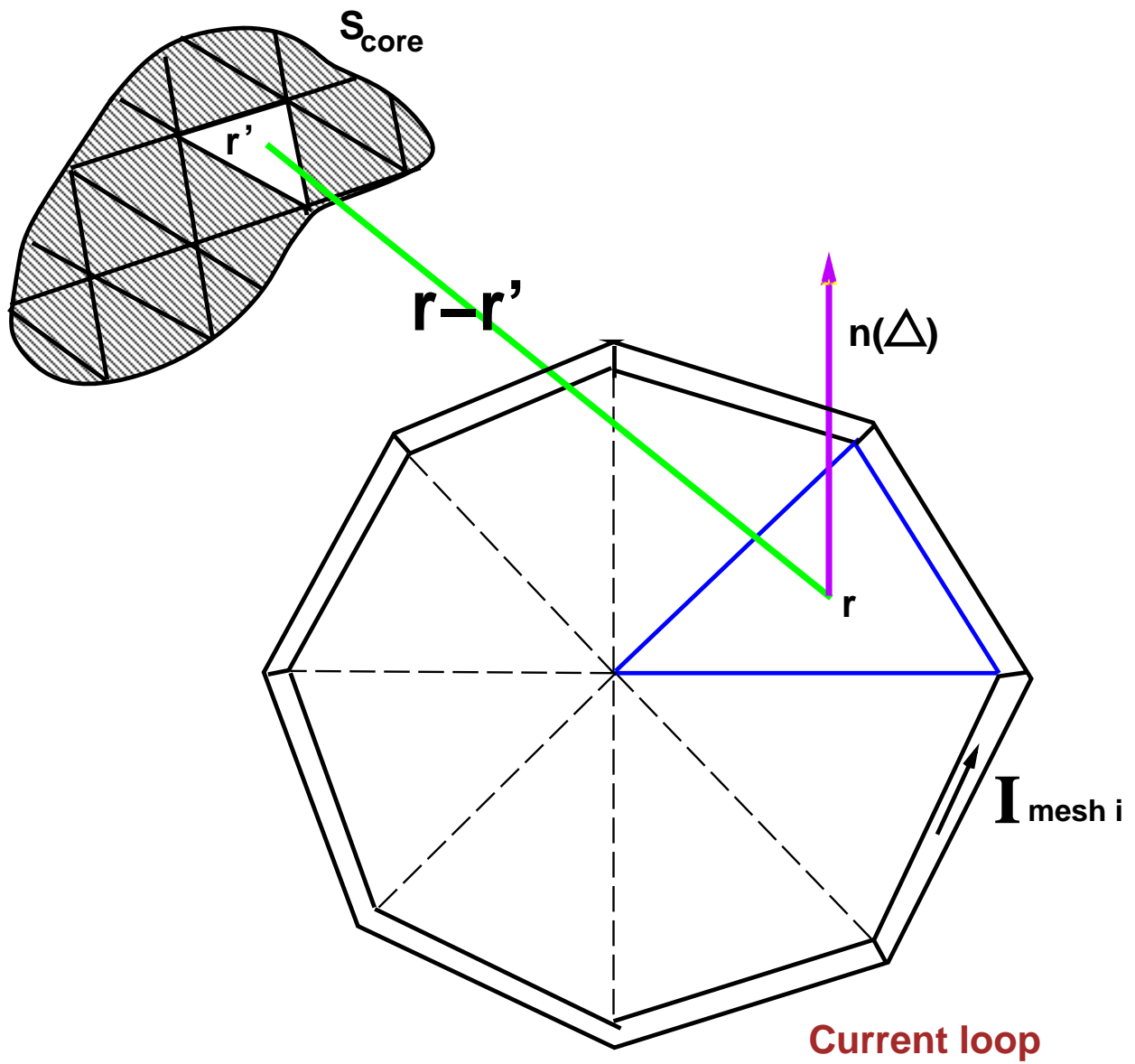
FIGURE 5-3: Evaluating $[L_\rho]_{ki}$, the effect of the magnetic charge of panel k of on mesh current i. Note that the surface of the current loop i are divided into triangles.

surface needs to be automated. For these reasons, $[L_\rho]_{ki}$ needs to be calculated in terms of the line integral along the current loop.

If we translate the surface of the loop to a new coordinate system such that the center of panel k is the origin of the new coordinate system, P_0. Thus, the integral in (5.8) becomes

$$[L_\rho]_{ki} = \frac{j\omega\mu_0}{4\pi} \int_{S_{mesh\ i}} \frac{1}{r^2} [u_r \cdot n(r)] dS \qquad (5.10)$$

where $n(r)$ is the normal the surface of current mesh i at point r and u_r is the unit vector along the r direction. The integral in (5.10) is equal to $\frac{j\omega\mu_0}{4\pi} I_\Omega(P_0)$, where $I_\Omega(P_0)$ is the solid angle integral. The solid angle integral is dependant only on the contour of the surface [60, 61, 62]. The solid angle integral $I_\Omega(P_0)$ is given by

$$I_\Omega(P_0) = \frac{1}{4\pi} \oint_C \left[\frac{Z(l)}{R(l)} - 1 \right] \frac{(\hat{\rho} \cdot \hat{v})(\hat{t} \cdot \hat{\eta})}{\rho} dL \qquad (5.11)$$

where R and Z are the two spherical coordinates of the point l on contour C, ρ is the projection of vector R on the x-y plane, $\hat{\rho}$ is the unit vector along ρ, $\hat{t}$ and $\hat{\eta}$ are the unit tangential vectors of the contour C and the projection curve of C on x-y plane, respectively, and $\hat{v} = \hat{\eta} \times \hat{z}$ with $\hat{z}$ being a unit vector along the z-axis. The geometry is shown in Figure 5-4.

Now we use the idea of the solid angle to get an efficient way to calculate $[L_\rho]_{ki}$

Thus, after translating the surface of the loop to a new coordinate system such that the center of panel k is the origin of the new coordinate system, P_0, $[L_\rho]_{ki}$ can be calculated as in

$$[L_\rho]_{ki} = \frac{j\omega\mu_0}{4\pi} \sum_{f=1}^{\#filaments\ in\ mesh\ i} \int_{L_{filament\ f}} \left[\frac{Z(l)}{R(l)} - 1 \right] \frac{(\hat{\rho} \cdot \hat{v})(\hat{t} \cdot \hat{\eta})}{\rho} dL$$

$$= \sum_{f=1}^{\#filaments\ in\ mesh\ i} E_{kf} \qquad (5.12)$$

77
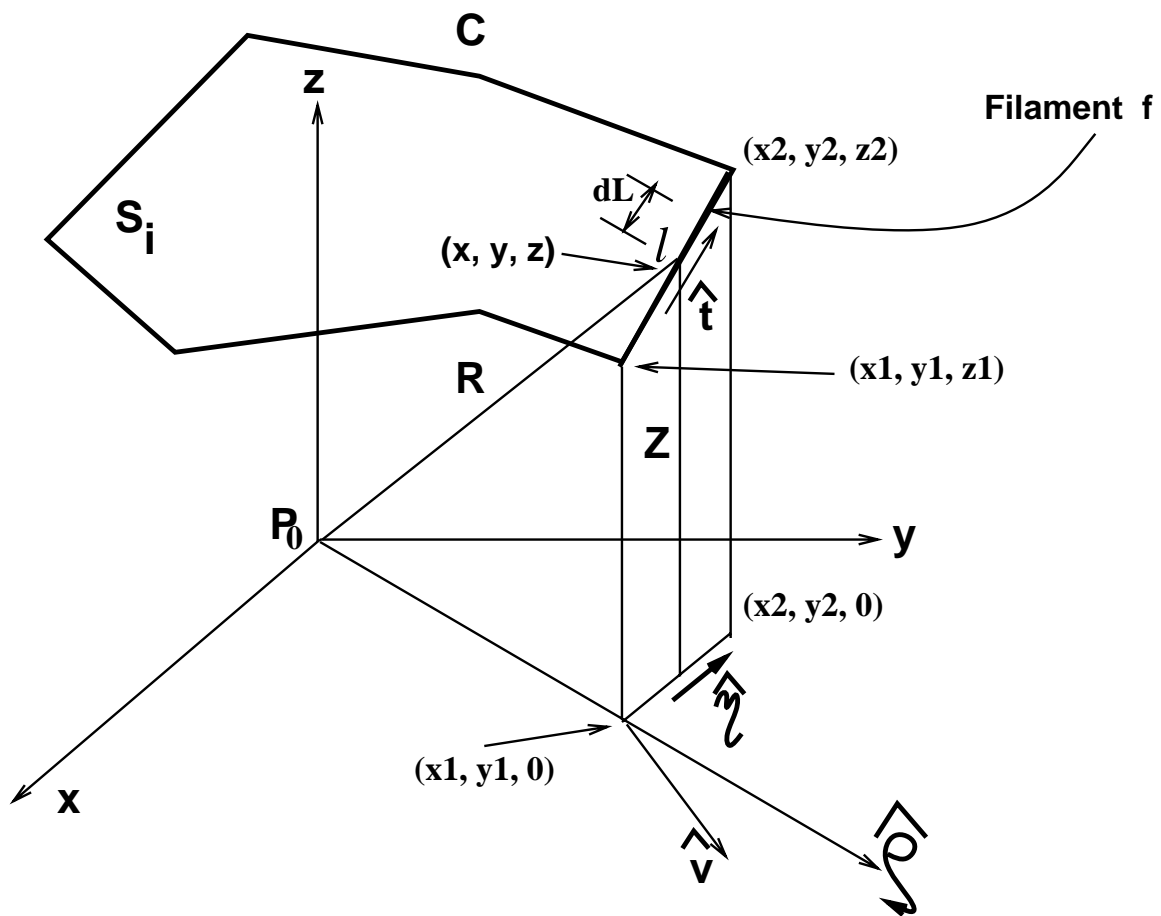
FIGURE 5-4: Evaluating of the solid angle integral at the origin P_0

After some mathematical manipulation, we get an expression for E_{kf} as in

$$E_{kf} = \frac{j\omega\mu_0}{4\pi} \int_l \left[\frac{z}{\sqrt{x^2 + y^2 + z^2}} - 1 \right] * \left[\frac{x(y_2 - y_1) - y(x_2 - x_1)}{(x^2 + y^2)} \right] *$$
$$\left[\frac{1}{(x_2 - x_1)^2 + (y_2 - y_1)^2 + (z_2 - z_1)^2} \right] dL \qquad (5.13)$$

where dL is a line integral along filament f,

$$x = x_1 + \left[\frac{(x_2 - x_1) * L}{(x_2 - x_1)^2 + (y_2 - y_1)^2 + (z_2 - z_1)^2} \right],$$

$$y = y_1 + \left[\frac{(y_2 - y_1)) * L}{(x_2 - x_1)^2 + (y_2 - y_1)^2 + (z_2 - z_1)^2} \right],$$

and

$$z = z_1 + \left[\frac{(z_2 - z_1)) * L}{(x_2 - x_1)^2 + (y_2 - y_1)^2 + (z_2 - z_1)^2} \right]$$

Note that (x_1, y_1, z_1) is the translated starting point of filament f and (x_2, y_2, z_2) is the translated end point of filament f, as shown in Figure 5-4.

The integral in (5.13) can be done using numerical quadrature [63]. We, thus, efficiently evaluate the elements of L_ρ in the linear system (4.49). The evaluation is used via a line integral along the length of the current meshes. This enables us to automate the integration process, and consequently, to handle complicated structure.

5.4 Evaluation of Magnetic Field due to magnetic charges

This section describes an efficient way to evaluate the elements of the sub-matrix Hn_ρ in the linear system (4.49). An element $[Hn_\rho]_{pk}$ is the magnetic field due to the magnetic charge of panel k, dotted with the unit normal to panel p, $n(p)$, as shown in Figure 5-5. The elements of Hn_ρ comes from (4.48) that resulted by discretizing the boundary condition equation (4.22) using the charges density approximation in (4.23).
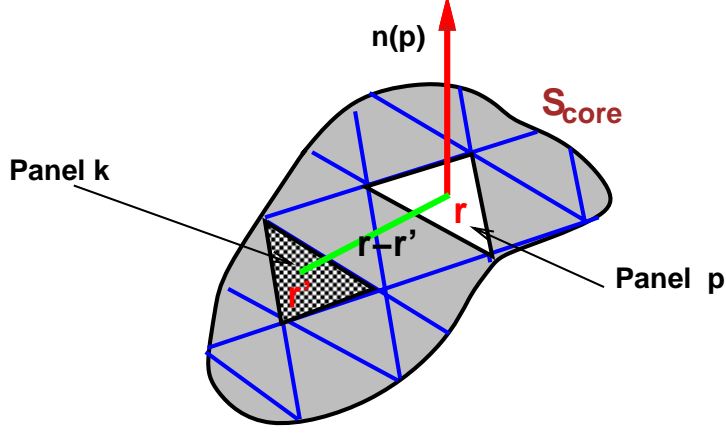
FIGURE 5-5: The surface of the permeable material is divided into triangles in calculating the integral Hn_ρ.

In the reminder of this section we test the possible discretization techniques for the boundary condition equation in order to accurately evaluate Hn_ρ. We begin by rewriting (4.22) as in,

$$\rho_m(p)\frac{2\pi(\mu_r+1)}{(\mu_r-1)} = H_C \cdot n(p) - \int_{S_{core}} \rho_m(r')n(p) \cdot \nabla \frac{1}{\mid r_p - r' \mid} dS', \qquad (5.14)$$

where ρ_m is the fictitious surface charge density, r_p and r' are positions in 3-space, μ_r is the relative permeability of the magnetic material, H_C is the magnetic field produced by free space current sources, S_{core} is the surface of the permeable material, and $n(p)$ is the normal to that surface at r_p.

5.4.1 Collocation and Galerkin Discretization

The integral equation in (5.14) can be solved by discretizing the permeable material's surface into panels on which the fictitious charge is assumed constant, and then determining the panel charges by enforcing (5.14) at test points. This discretization produces the following collocation equation,

$$\frac{q_k}{A_k}\frac{2\pi(\mu_r+1)}{(\mu_r-1)} = H_C \cdot n(p) - \sum_k \frac{q_k}{A_k} \int_{S_k} n(p) \cdot \nabla \frac{1}{\mid r_p - r' \mid} dS' \qquad (5.15)$$

where q_k is the fictitious magnetic charge on the kth panel on the magnetic material surface, A_k is area of the kth panel on the magnetic material surface, n_p is the unit vector

normal to the magnetic material surface calculated at the center of panel k, and S_k is the surface of panel k. If the surface is discretized into flat triangles, the integral in (5.15) can be calculated analytically [58] . Consequently, using the collocation method is efficient.

The galerkin approach can also be used to discretized (5.14), in which case the panel charges are determined by enforcing (5.14) in average over a panel. This discretization produces the following galerkin equation,

$$\frac{q_k}{A_k} \frac{2\pi(\mu_r+1)}{(\mu_r-1)} = H_C \cdot n(p) - \frac{1}{A_p} \frac{q_k}{A_k} \int_{S_p} \int_{S_k} n(p) \cdot \nabla \frac{1}{|r_p - r'|} dS'_k dS_p \qquad (5.16)$$

where A_p is the surface area of panel p.

The double integral in the galerkin method (5.16) is harder to evaluate than the integral in the collocation method (5.15), and is typically computed by combining analytic integration with numerical quadrature.

5.4.2   Qualocation Discretization

If the collocation method with a coarse discretization is used to solve (5.14), the computed fictitious charges are quite inaccurate when dealing with permeable material with edges. Switching to the galerkin method improves accuracy substantially, but the galerkin method is more expensive. Instead, we show that by using a qualocation method [64, 65], which costs no more than collocation, the fictitious charges are also accurately computed.

Like the collocation method, the qualocation method can be thought of as an approximation to the galerkin method. In qualocation, however, the panel charge is approximated as a point charge and the integral equation is enforced in average over a panel. This results in the following qualocation equation,

$$\frac{q_k}{A_k} \frac{2\pi(\mu_r+1)}{(\mu_r-1)} = H_C \cdot n(p) - \frac{A_k}{A_p} \sum_k \frac{q_k}{A_k} \int_{S_p} n(p) \cdot \nabla \frac{1}{|r - r'_k|} dS' \qquad (5.17)$$

The integral in the qualocation method (5.17) is equivalent to computing a dipole potential, and can be evaluated analytically [58]. Thus amount of work needed to compute the fictitious magnetic surface charge, and therefore, field and inductance values, is
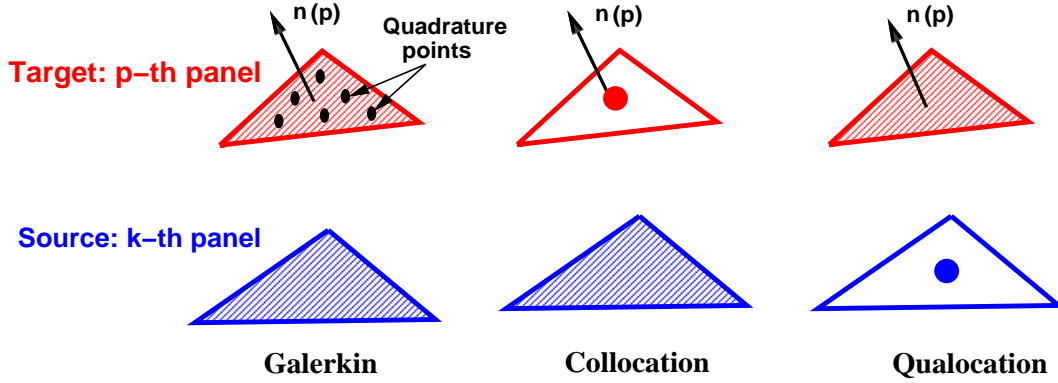
FIGURE 5-6: Different discretization configurations

almost the same when using the collocation or qualocation method. Figure 5-6 shows a schematic for the three different discretization methods. The galerkin method is represented by two shaded triangles because the galerkin integral in (5.16) is evaluated over both the source and the target triangles. While, the inner integral in the galerkin integral, on the source panel, is calculated analytically, the outer integral in the galerkin integral, on the target panel, is approximated using quadrature points.

In the collocation method, the target triangle is not shaded because the integral in (5.16) is approximated at the target triangle's centroid. However, in the qualocation method, the source triangle is not shaded because the integral over the source triangle is approximated as a point charge at the its centroid.

After computing the magnetic charges, the total magnetic field can be calculated from

$$H(r)_{Total} = H_C - \sum_k \frac{q_k}{A_k} \int_S \nabla \frac{1}{\mid r - r' \mid} dS'_k. \qquad (5.18)$$

5.4.3   Qualocation Accuracy Results

In order to compare the accuracy of the three discretization techniques, consider the two adjacent perpendicular panel shown in Figure 5-7. Figure 5-8 compares the error in computing the integral in (5.14) using the three discretization methods. For this example, the collocation method produced more than 33% error. The qualocation method produced only 1% error which can be achieved only by using eight point quadrature in
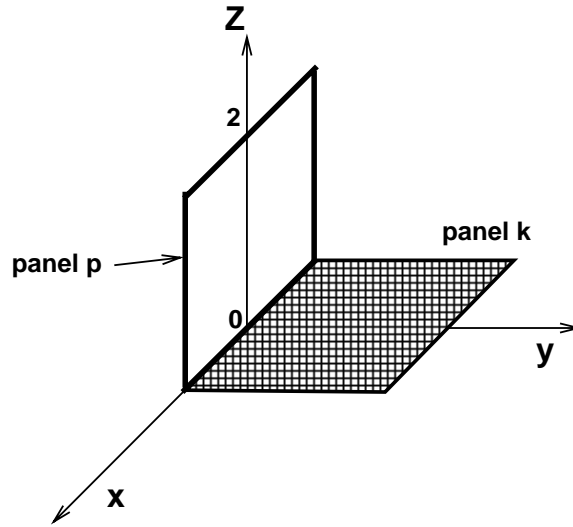
FIGURE 5-7: Two adjacent panels
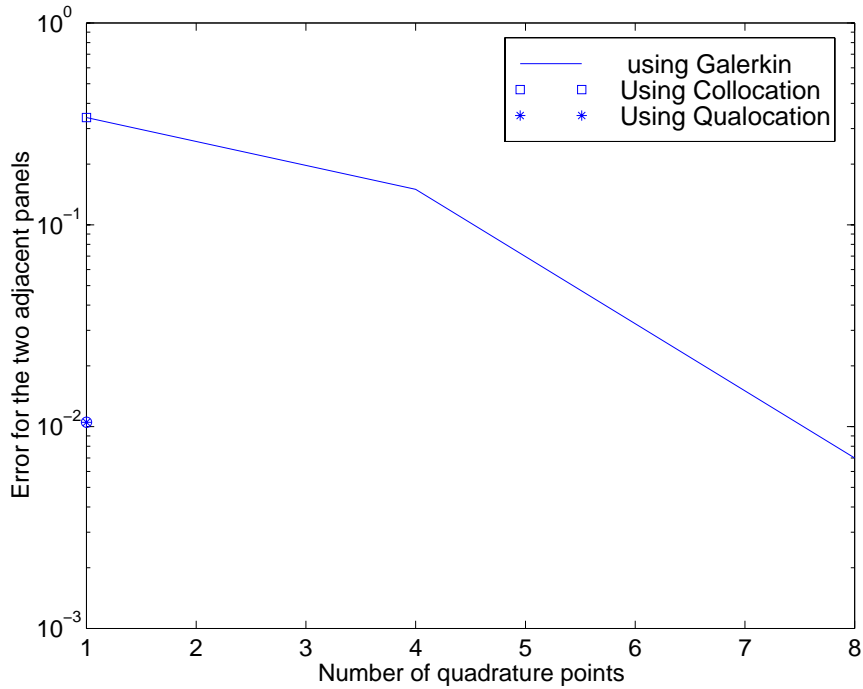
FIGURE 5-8: Accuracy comparison of the three discretization techniques in the two panel example

the galerkin integral. The collocation integral, $\int_{S_k} n(p) \cdot \nabla \frac{1}{|r_p - r'|} dS'$, is effectively the field at an evaluation point, at panel p, due to the charge on panel k dotted with the normal at panel p. Figure 5-9 shows the field on the z axis on panel p due to the charge on panel k for the two panel example Figure 5-7. As shown in Figure 5-9, the field blows

83
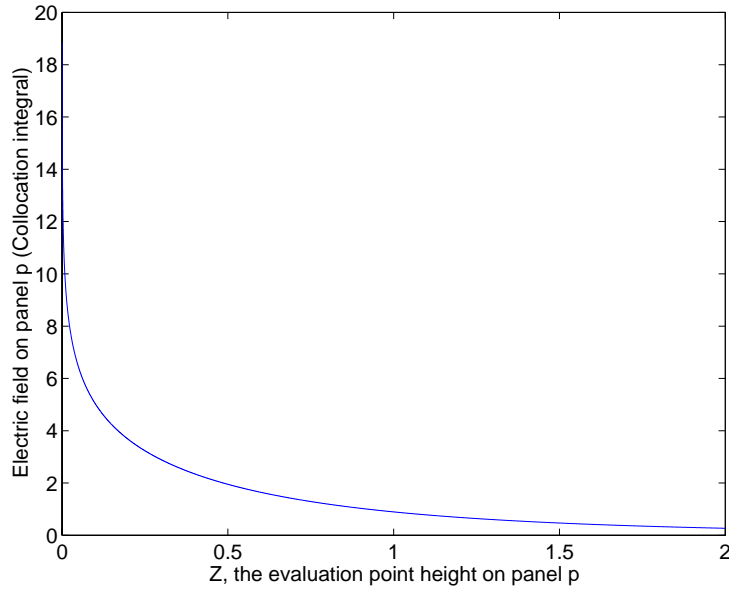
FIGURE 5-9: Evaluation of the electric field as the evaluation point on panel p approaches the charge panel k in the two panel example

up as the evaluation point on panel p approaches the charge layer of panel k.

On the other hand, the qualocation integral $\int_{S_p} n(p) \cdot \nabla \frac{1}{|r - r'_k|} dS'$ is effectively the the potential, at panel p, due to the dipole charge layer of panel k. Figure 5-10 shows the potential on the z axis on panel p due to the dipole charge layer of panel k in the two panel example. As shown in Figure 5-10, the dipole potential is always bounded no matter how close the evaluation point is to the charge panel.

Thus, the qualocation integral is much better behaved than the collocation integral when the evaluation point is close to charge panel. This explains why qualocation is much more accurate than collocation specially when dealing with edges.
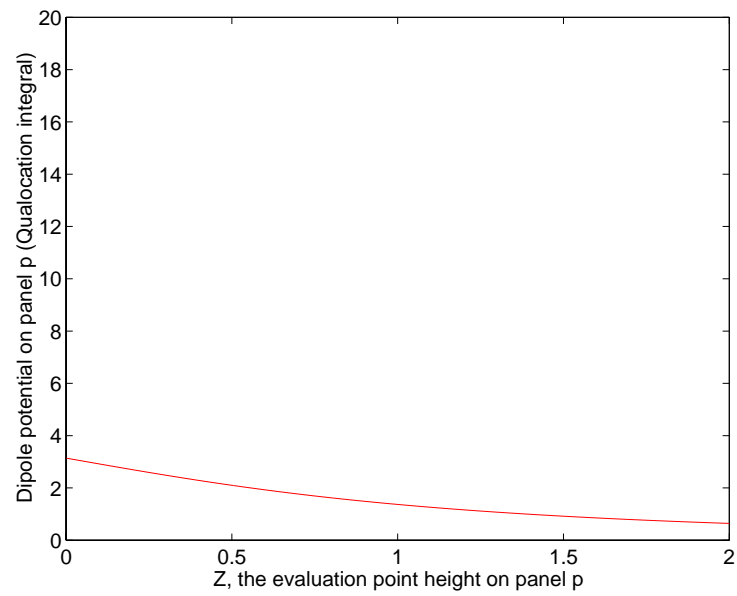
FIGURE 5-10: Evaluation of the dipole potential as the evaluation point on panel p approaches the dipole charge panel k in the two panel example

6

Algorithm Results

6.1 Algorithm Accuracy Results

In this chapter, we present computational results compared with published or analytical data to demonstrate the accuracy and versatility of the algorithm.

We first start by demonstrating the accuracy of the qualocation method. We examined the problem of permeable material in a uniform vertical magnetic field shown in Figure 6-1. We used our algorithm to compute the magnetic charge density on the permeable material. We then calculated the average field across the cylinder's median cross section and compared with the published data in [66, 67, 68, 69]. Figure 6-2 shows the distribution of the surface magnetic charge density on the cylinder produced by our algorithm. This distribution was then used to compute the average flux density over the median cross section of the cylinder shown in Figure 6-3. The average flux density over the median cross section of the cylinder, computed using the qualocation method matches the exact solution much more accurately than when using the collocation method, with larger differences associated with higher permeability.

In order to test the effect of the aspect ratio of the permeable structure on accuracy of the algorithm, we examined the analytically solvable problem of an ellipsoid of permeable material in a uniform vertical magnetic field, shown in Figure 6-4. We used our algorithm to compute the magnetic charge density on the permeable material, as shown
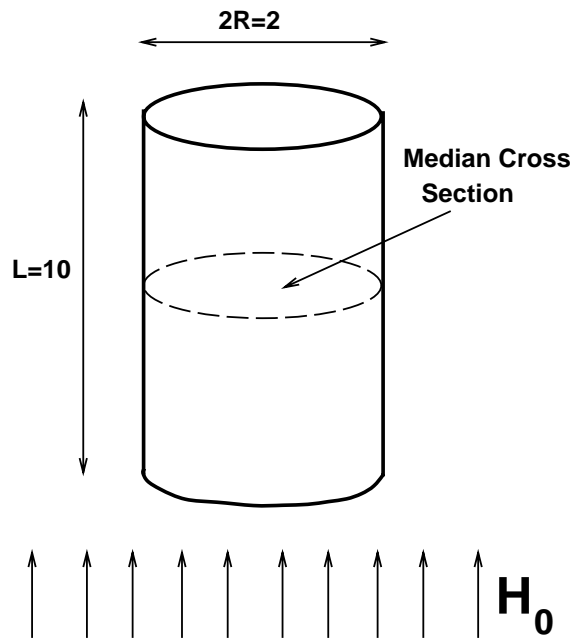
FIGURE 6-1: Permeable Cylinder in Ho

Charge Density
2.34435E+06
2.25192E+06
2.1595E+06
2.06708E+06
1.97465E+06
1.88223E+06
1.78981E+06
1.69739E+06
1.60496E+06
1.51254E+06
1.42012E+06
1.32769E+06
1.23527E+06
1.14285E+06
1.05043E+06
958002
865579
773156
680733
588311
495888
403465
311042
218619
126196
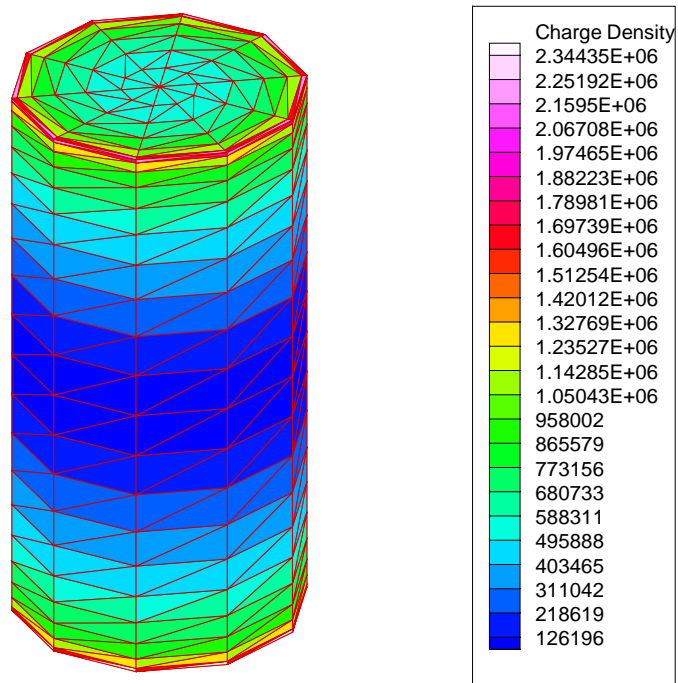
FIGURE 6-2: Magnetic surface charge distribution on the permeable cylinder of $\mu = 10$
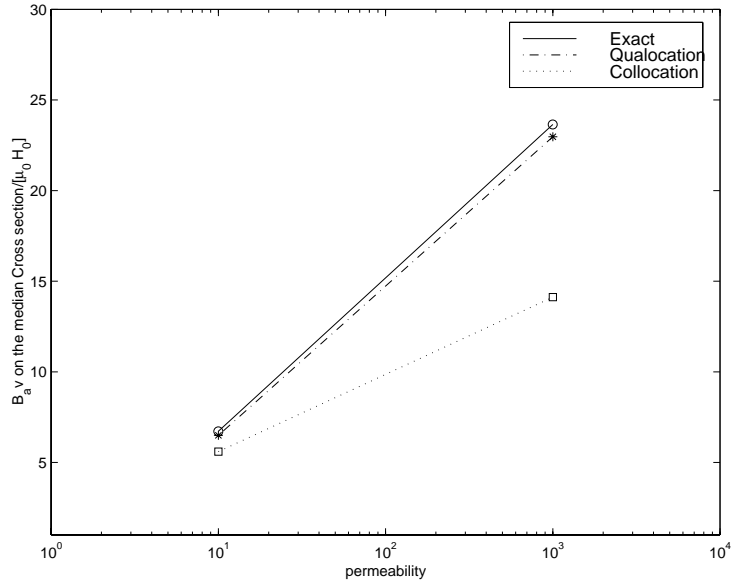
FIGURE 6-3: Average flux density over the permeable cylinder's median cross section, for different permeabilities. Note that 960 panels were used to discretize the cylinder
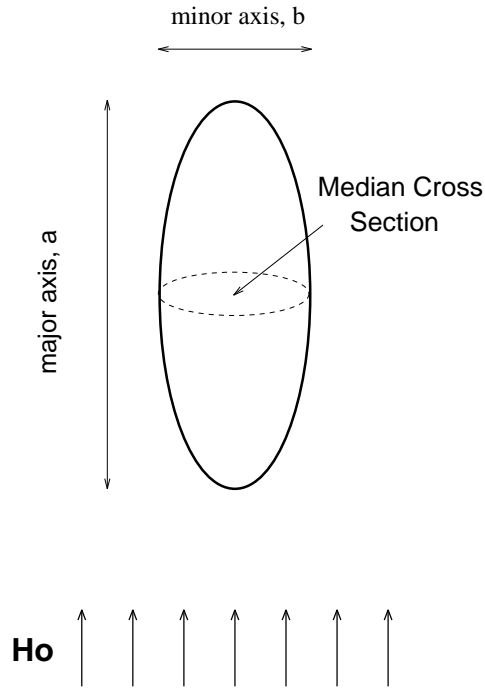
FIGURE 6-4: Ellipsoid with $\mu_r = 1000$ in Ho, b=1 m.

in Figure 6-5. We then calculated the average field across the median cross section of the permeable ellipsoid and compared it with the analytical results [70, 71]. As shown in Figure 6-6, the average flux density over the median cross section of the ellipsoid, shown

mu=1000
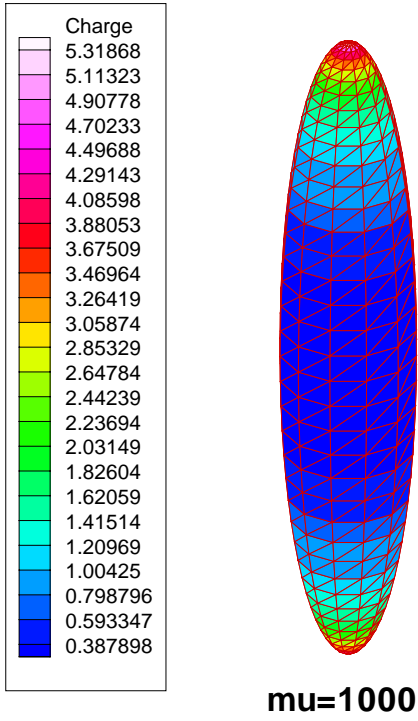
FIGURE 6-5: Magnetic surface charge distribution on a high aspect ratio permeable ellipsoid of $\mu = 1000$
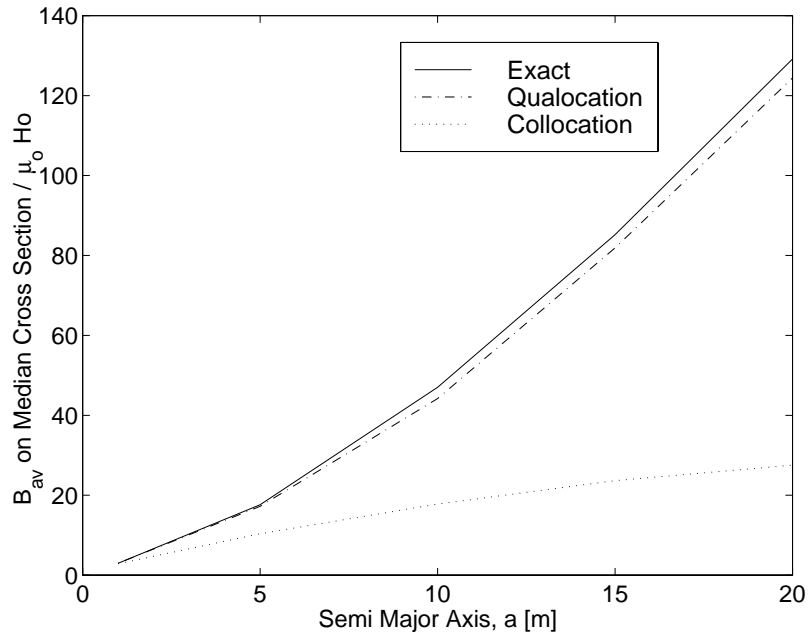
FIGURE 6-6: Average flux density over the ellipsoid's median cross section, for different aspect ratios
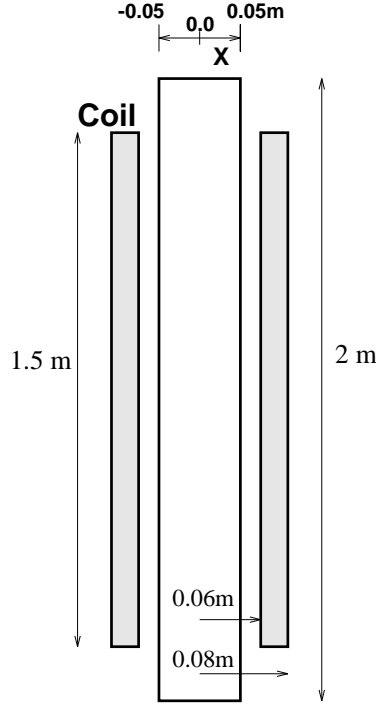
FIGURE 6-7: Coil surrounding $\mu_r = 1000$ cylinder.
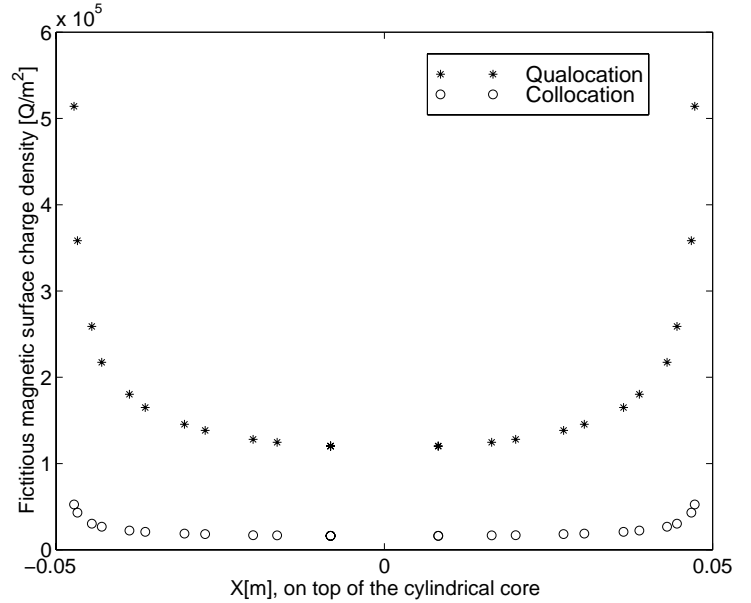
FIGURE 6-8: Fictitious magnetic surface charge on cylinder top.

in Figure 6-4, computed using the qualocation method matches the analytic solution much more accurately than when using the collocation method, with larger difference associated with thinner ellipsoids.

The inaccuracy of the collocation approach is most clearly demonstrated by examining a coil of wire around a long permeable cylinder, shown in Figure 6-7. Figure 6-8 shows that the collocation underestimates the magnetic charges on top of the permeable cylinder. Qualocation method is no more expensive than collocation and is much more accurate for highly permeable materials with big aspect ratio or with edges.

An example to demonstrate the accuracy of the algorithm is the example of a spiral inductor over a permeable material substrate. These planar inductors have been studied for some time [72, 73, 74, 75, 4]. The tested realistic spiral inductor in Figure 6-9 has a diameter of 280μ, with a 10μ by 10μ cross section. The permeable material substrate is 1500μ by 1500μ, with 200μ as its thickness.

Figure 6-10 shows the variation of extracted inductance with the permeability of the permeable substrate. The inductance of the spiral inductor over a magnetic substrate
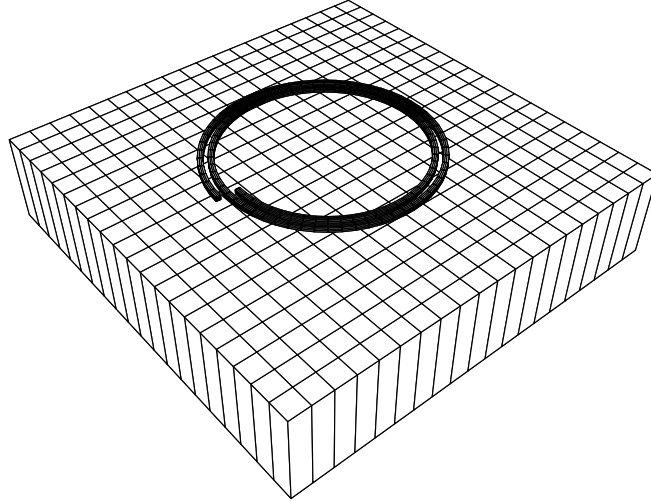
FIGURE 6-9: A spiral inductor over a magnetic substrate.
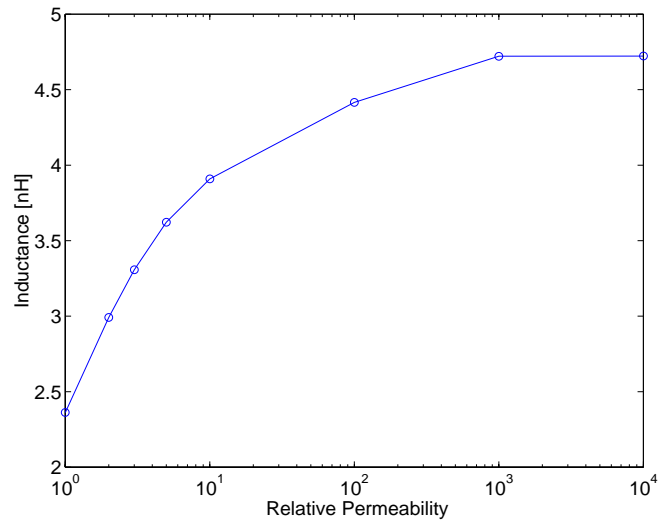
FIGURE 6-10: Variation of the inductance of spiral inductor with relative of the magnetic substrate.

increases as the permeability increases, till it reaches an upper limit which is almost double the value of the spiral inductance without a substrate [74, 75].

Figure 6-11 shows the frequency response of the inductance of the spiral inductor in Figure 6-9. Note the high frequency inductance is lower than the low frequency one, due to the skin effect. The frequency at which the inductance start to drop is mainly determined by the size of the cross section of the conductor.
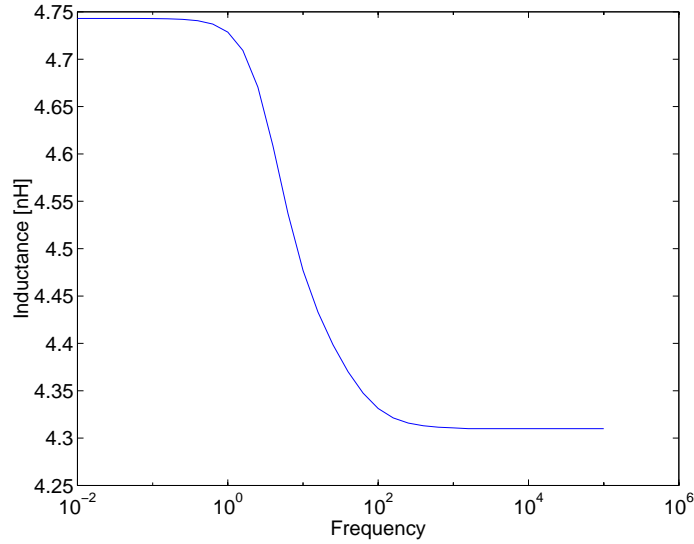
FIGURE 6-11: Inductance frequency response of the spiral inductor over a magnetic substrate example. The substrate has a relative permeabilty of 2000.

Algorithm 6.2.1 (GMRES Algorithm for Ax = b).

```
guess x⁰
for  k = 0, 1, … until converged {
    Compute the error, rᵏ = b − Axᵏ
    Find xᵏ⁺¹ to minimize rᵏ⁺¹
        based on xⁱ and rⁱ,  i = 0, … , k
}
```

6.2   Algorithm Computational Results

The standard method to solve the linear system in (4.49) is Gaussian elimination [76, 77, 78] but the computational cost is m^3 operations, which is expensive and sometimes impractical for complicated structures. For this reason we use a conjugate-residual style iterative method like GMRES [79]. Such methods have the general form given in Algorithm 6.2. The cost of the GMRES algorithm is order m^2 operations per iteration and in order to reduce the number of iterations a preconditioner is usually needed.

In general, however, the GMRES iterative method applied to solving (4.49) can be significantly accelerated by preconditioning if there is an easily computed good approximation, P to the inverse of system matrix. Using preconditioning the GMRES algorithm

93

is equivalent to using GMRES to solve

$$\begin{bmatrix} R(\omega) + j\omega L_J(\omega) & j\omega L_\rho(\omega) \\ Hn_J & (Hn_\rho - I) \end{bmatrix} [P][x] = \begin{bmatrix} V \\ 0 \end{bmatrix} \qquad (6.1)$$

for the unknown vector x. Then we compute $\begin{bmatrix} \overline{I}_M \\ \overline{q}_k \end{bmatrix} = Px$. Clearly, if P is precisely equal to inverse of the system matrix, then (6.1) is trivial to solve, but then P will be very expensive to compute.

Since the individual elements in the sub-matrix Hn_ρ in (4.49) decay like $\frac{1}{r^2}$, the sub-matrix $[Hn_\rho - I]$ are diagonally dominated. Note that the diagonal elements of Hn_ρ are zeros, thus, the identity matrix produces a good approximation of the sub-matrix $[Hn_\rho - I]$. The elements of coupling sub-matrix Hn_J are the field values on the panels. These values are at best of the same order as the elements of Hn_J which is dominated by the identity. Moreover, the elements of the sub-matrix $j\omega L_\rho$ decay like $\frac{1}{r^2}$ which is much faster than the $\frac{1}{r}$ decay of the elements of $j\omega L_J$. Thus, the sub-matrices Hn_J and $j\omega L_\rho$ are small and could be canceled in the preconditioner and a good choice for the preconditioner P can be:

$$P = \begin{bmatrix} lp^{-1} & 0 \\ 0 & -I \end{bmatrix} \qquad (6.2)$$

where lp^{-1} is a good approximation to the sub-matrix $[R(\omega) + j\omega L_J(\omega)]^{-1}$

By using (5.3), $[R(\omega) + j\omega L_J(\omega)] = [MR_p(\omega)M^t + j\omega ML_pM^t(\omega)]$, where R_p is the diagonal resistance matrix, L_p is the partial inductance matrix, and M is the sparse mesh matrix. If we get a sparsified approximation of L_p, we can then get a sparse matrix lp, and thus a sparse preconditioner, P, using (6.2) will be formed.

First sparse approximation of L_p that comes to mind is the diagonal of L_p which is the sparsest approximation of L_p .

Because many of the structures that contain permeable material uses long current loops causes the interaction between the filaments in the same segment to be much bigger than the interaction between a filament in this segment and filaments in other

94
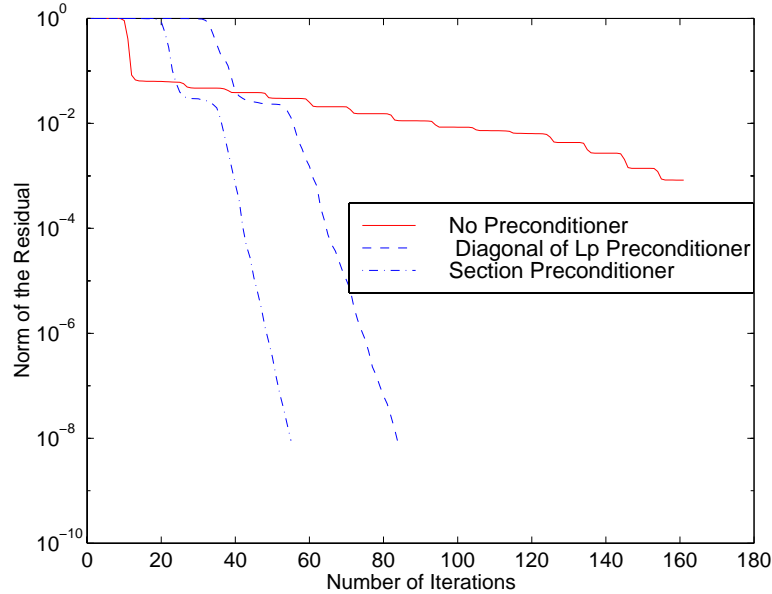
FIGURE 6-12: Convergence of GMRES using different preconditioners, for the problem of the cylindrical inductor with permeable core. The linear system size is 1765 by 1765.

segments. This suggests the use of a section block diagonal approximation [56]. In this approximation, we include only the principle sub-matrices of L_p corresponding to the groups of filaments contained in each segment. For example, the one conductor circuit shown in Figure 4-3, the section block diagonal approximation of L_p would consist of two 2×2 blocks.

Figure 6-12 compares the GMRES convergence rate of the preconditioners, when extracting the inductance of of the cylindrical coil with permeable core shown in Figure 6-7. We see that section preconditioner converges faster than the diagonal of L_p method and that both of them are much faster GMRES with no preconditioner.

Figure 6-18 shows the number of GMRES iterations needed to extract the inductance of the cylindrical coil with permeable core shown in Figure 6-7. As it is illustrated Figure 6-18, using a preconditioner significantly reduced the number of iterations in the GMRES algorithm. A good preconditioner helps keep the number of iterations almost constant with the increase of the number of unknowns, as it is the case for the section block diagonal preconditioner.

The faster convergence of GMRES when using the section block diagonal precondi-
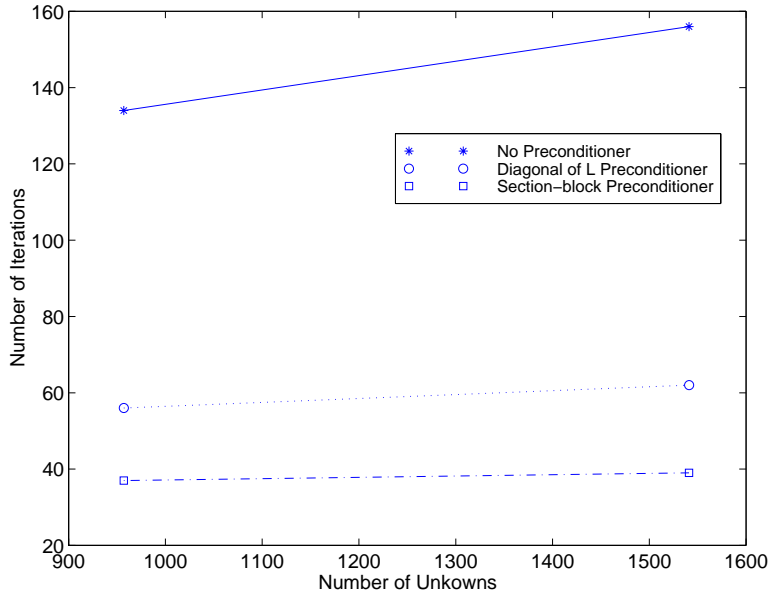
FIGURE 6-13: Effect of preconditioner on the number of iterations used in GMRES for the cylindrical inductor example.
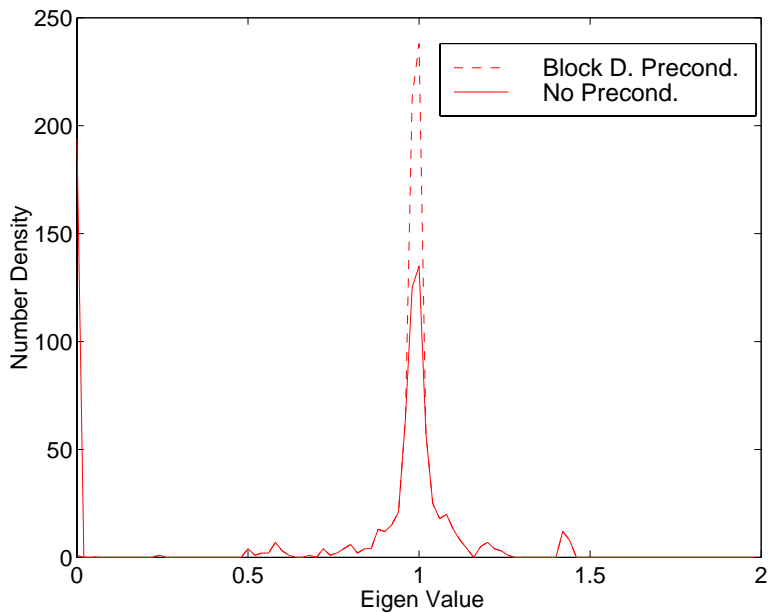
FIGURE 6-14: Eigen values for the preconditioned system and the un-preconditioned system. Note the many near-zero eigen values for the un-preconditioned system

tioner can be explained by examining the spectra of the preconditioned matrix and the un-preconditioned matrix in Figure 6-14. The eign values for the preconditioned are much more clustered than in the un-preconditioned system. Moreover, the number of
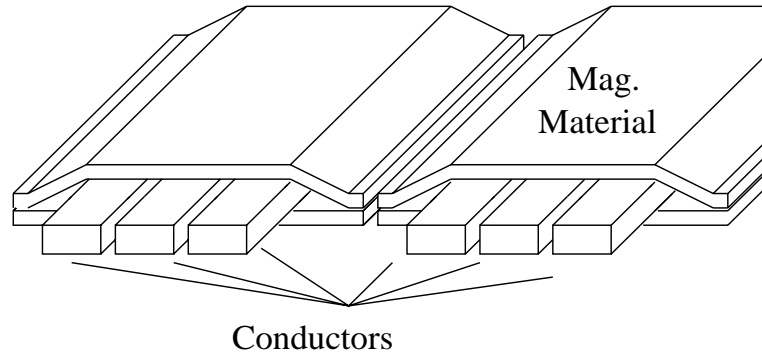
FIGURE 6-15: Side view of the microfabricated inductor

FIGURE 6-16: Top view of the multi layer core microfabricated inductor

near-zero eign values of the un-preconditioned system is much more than those of the preconditioned system. These near zero eign values increases the condition number of the matrix and thus causes slower convergence [76]. Note that the condition number of a matrix is equal to biggest eign value divided by the smallest eigen value.

We used the industrial example of a microfabricated inductor in [80] to further test the convergence rate of our preconditioned GMRES algorithm. The microfabricated inductor is shown in Figure 6-15, 6-16. We used the section block diagonal preconditioner to accelerate the convergence rate of GMRES. For a resulting linear system of 2905×2905, the section preconditioner significantly improved the convergence compared to no preconditioner case, as shown in Figure 6-17.

In Figure 6-13, we show the CPU time consumed when solving the cylindrical inductor with the preconditioned GMRES method or with the standard direct methods, such as Gaussian Elimination. Figure 6-13 shows that preconditioned GMRES method using the section preconditioner, is up to an order of magnitude faster than standard Gaussian Elimination method.
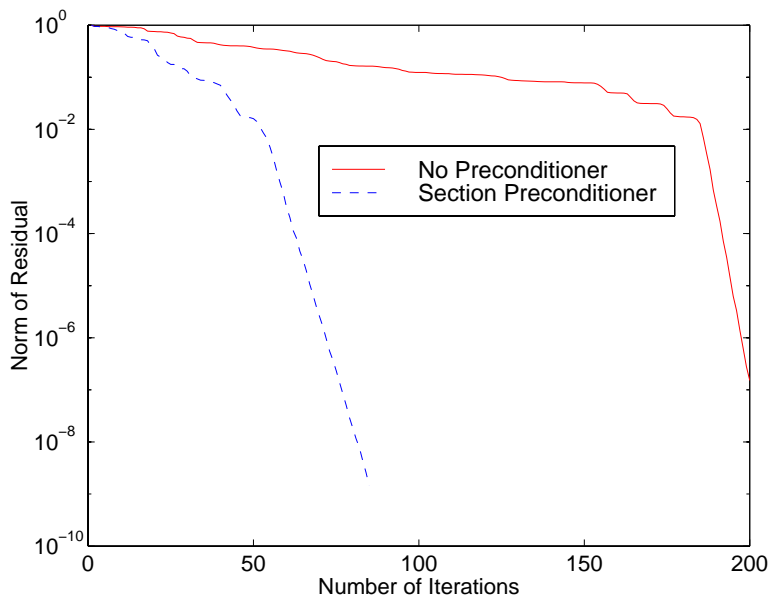
FIGURE 6-17: Much Improved GMRES convergence rate when using section preconditioner for the microfabricated inductor
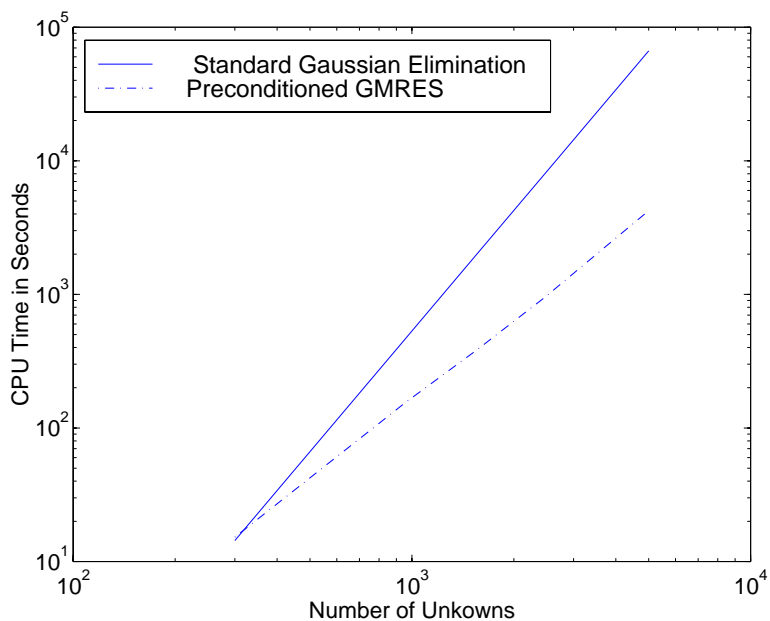
FIGURE 6-18: Comparison between the CPU times consumed in the preconditioned GMRES method and in the standard direct method.

Conclusion and Future Work

7.1   Summary

In this thesis, we have investigated several algorithms for accurate simulation of inductive effects. The first part of the thesis dealt with the analysis of on-chip interconnect inductive effects. It first investigated the interconnect coupling inductance and its effect on circuit crosstalk. In order to accurately model the effect of the substrate on the coupling inductance and examine the standard approach of dealing with the semiconductor substrate effect, the substrate was simulated using a full 3-D mesh of filaments.

We showed that, at frequencies below 20 gigahertz, it is the much larger *low* frequency inductance that is important. We also showed that the standard ideal ground plane technique failed to predict coupling inductance for frequencies below 20 gigahertz and it underestimated the value of the actual coupling inductance by up to four times. The effect of the interconnect coupling inductance on circuit cross-talk has been shown. A method for the reduction of the coupling inductance was also proposed.

Part I then analyzed the minimization of the interconnect self inductance, and therefore, reducing its effect on signal delay and delay skew. We showed that, for integrated circuit operating at below twenty-five gigahertz, it is the low frequency inductance that predicts the performance. We then compared the performance of the sandwiched structure, using two dedicated ground planes, and interdigitating thinned signal lines with

thinned ground lines. Our results demonstrate that the interdigitated approach reduced interconnect self inductance by more than a factor of four over the other techniques, for a modest rise in capacitance, resistance and area.

In the second part of the thesis, we developed a fast algorithm to efficiently extract the frequency dependent inductance for 3-D structures that contain linear permeable materials. This algorithm avoids numerical cancellation errors by calculating fields outside of the permeable material.

The algorithm uses a magnetic surface charge formulation, with very efficient techniques for evaluating the required integrals using either analytical techniques or efficient quadrature methods. A qualocation discretization technique was used and was proven to be no more expensive and up to an order of magnitude more accurate than standard collocation for highly permeable materials with big aspect ratios or with edges. Computational results were presented and compared with experimental data to demonstrate the accuracy of our algorithm. The resulting system is solved iteratively using a preconditioned GMRES method that is up to an order of magnitude faster than the standard direct method, and therefore, allows the analysis of complicated structures.

7.2   Future Work

Part II derived a computationally efficient method for inductance extraction in presence of linear magnetic materials. Although many of the MEMS applications use linear magnetic material, some applications use non-linear permeable materials. The algorithm may be extended to handle non-linear permeable materials by introducing a scalar volumetric magnetic charge inside the magnetic material, along with the surface magnetic charge. A non linear system of equations may be generated and then solved using Newton method.

A

Effect of Air Gap on Extracted Inductance in Magnetic Circuits

The magnetic formulation derived, in part II of the thesis, deals with magnetic circuits that contain air gaps. In this appendix, we demonstrate the effect of the air gap in magnetic circuits on the extracted inductance by our magnetic formulation. We used the formulation to solve the problem of the toroidal inductor shown in Figure A-1.

It is well known that as the length air gap decreases, the inductance increases. If the length of the air gap is small compared to the length of the magnetic circuit divided by the relative permeability of the magnetic material, the inductance will no longer be affected by the air gap and it will saturate to a fixed value [28].

Figure A-2 shows that, when using 944 panels to discretize the toroid, the extracted inductance of the toroidal inductor fits well with the theory, that the inductance increases as the length of the air gap decreases. However, when the air gap length became less than the length of the magnetic circuit divided by the relative permeability of the magnetic material, the formulation failed to capture the right inductance, as the inductance starts to decay rather than saturating to the limiting value. As also shown in Figure A-2, the extracted inductance in the case of zero air gap is far from the saturated value, and thus the formulation may be inaccurate if used for closed magnetic circuits.

When a finer discretization is used, the length of the air gap at which the formulation fails became smaller, as shown in Figure A-2. Thus, closed magnetic circuits could be
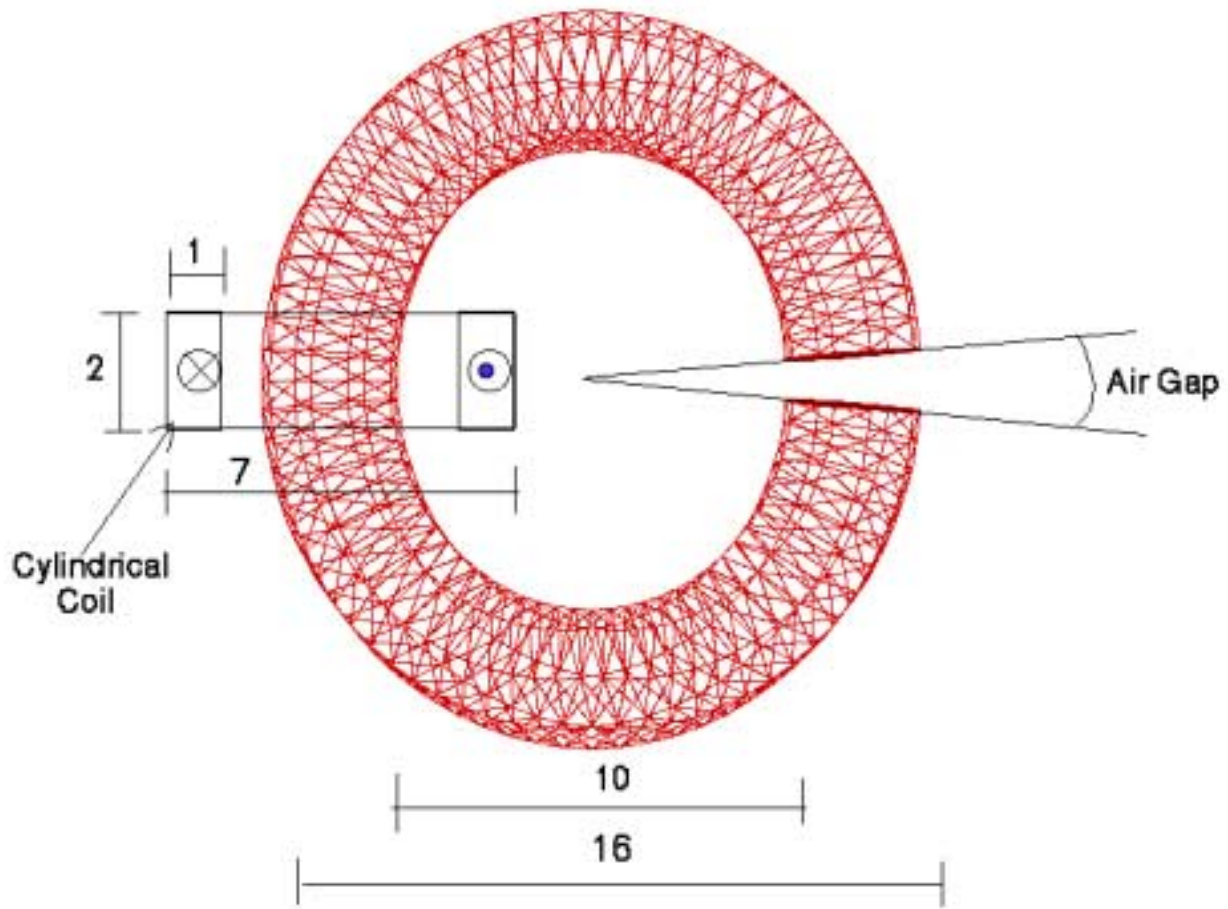
FIGURE A-1: C Toroidal Inductor. Note that $L = 2 * \pi * R$, where R is the radius of the toroidal inductor and equal to 6.5m

analyzed using the formulation, if a thin air gap is introduced. This air gap has to be small enough so that it doesn't affect the value of the inductance, but in the same time, the discretization has to be fine enough to be predict the saturated inductance.
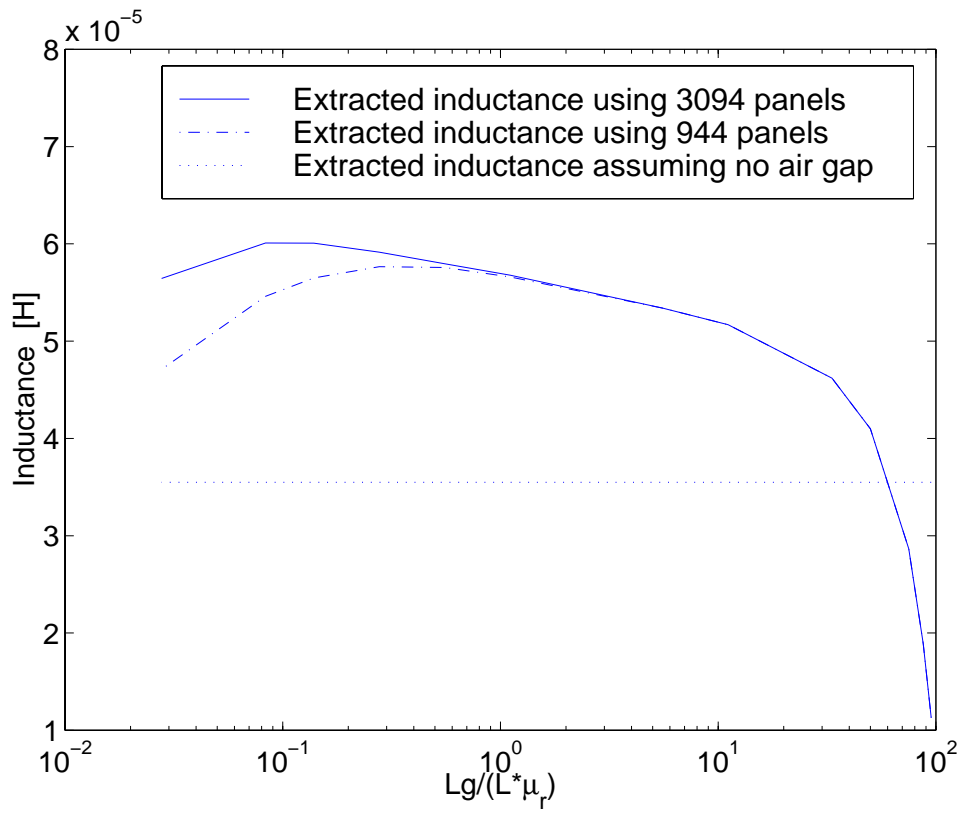
FIGURE A-2: Extracted inductance of the toroidal inductor

Bibliography

[1] D. A. Priore, "Inductance on Silicon for Sub-Micron CMOS VLSI," in *Proc. IEEE Symposium on VLSI Circuits*, 1993.

[2] L. Pileggi, "Coping with RC(L) Interconnect Design Headaches," in *Proc. of the International Conference on Computer-Aided Design*, October 1995.

[3] H. Guckel, T. Christenson, K. Skrobis, T. Jung, J. Klein, K. Hartojo, and I. Widjaja, "A first functional current excited planar rotational magnetic micromotor," *IEEE Transactions on Micro-Electromechanical Systems*, pp. 7–11, January 1993.

[4] W. Hurley, M. Duffy, S. Oreilly, and S. Omathuna, "Impedance formulas for planar magnetic structures with spiral windings," *IEEE Transactions on Industrial Electronics*, pp. 271–276, April 1999.

[5] C. Ahn and M. Allen, "Micromachined planar inductors on silicon wafers for mems applications," *IEEE Transactions on Industrial Electronics*, pp. 866–876, December 1998.

[6] K. Shirakawa, K. Yamaguchi, M. Hirata, T. Yamaoka, F. Takeda, K. Murakami, and H. Matsuki, "Thin film cloth-structured inductor for magnetic integrated circuits," *IEEE Transactions on Magnetics*, pp. 2262–2264, September 1990.

[7] C. Ahn, Y. Kim, and M. Allen, "A fully integrated planar toroidal inductor with a micromachined nickel-iron magnetic bar," *IEEE Transactions on Components Packaging and Manufacturing Technology Part A*, pp. 463–469, September 1994.

[8] R. Soohoo, "Magnetic thin film inductors for integrated circuit applications," *IEEE Transactions on Magnetics*, pp. 1803–1805, November 1979.

[9] W. Taylor, M. Allen, and C. Dauwalter, "A fully integrated magnetically actuated micromachined relay," in *Technical Digest the Solid-State Sensor and Actuator Workshop*, June 1996.

[10] C. Ahn and M. Allen, "A fully integrated surface micromachined magnetic microactuator with a multilevel meander magnetic core," *Journal of Micromechanics and Microengineering*, pp. 15–22, March 1993.

[11] W. Taylor, O. Brand, and M. Allen, "Fully integrated magnetically actuated micromachined relays," *Journal of Microelectromechanical Systems*, pp. 181–191, June 1998.

[12] C. Ahn and M. Allen, "A fully integrated micromagnetic actuator with a multilevel meander magnetic core," in *Technical Digest the Solid-State Sensor and Actuator Workshop*, June 1992.

[13] C. Ahn and M. Allen, "A planar micromachined spiral inductor for integrated magnetic microactuator applications," *Journal of Micromechanics and Microengineering*, pp. 37–44, June 1993.

[14] C. Sullivan and S. Sanders, "Design of microfabricated transformers and inductors for high-frequency power conversion," *IEEE Transactions on Power Electronics*, pp. 228–238, February 1996.

[15] T. Sato, H. Tomita, A. Sawabe, T. Inoue, T. Mizoguhci, and M. Sahashi, "A magnetic thin film inductor and its application to a MHZ switching dc-dc converter," *IEEE Transactions on Micro-Electromechanical Systems*, pp. 217–223, March 1994.

[16] K. Yamaguchi, S. Ohnuma, T. Imagawa, J. Toriu, H. Matsuki, and K. Murakami, "Characteristics of a thin film microtranformers with spiral inductor coils," *IEEE Transactions on Magnetics*, pp. 2232–2237, May 1993.

[17] K. Yamaguchi, E. Sugawara, O. Nakajima, and H. Matsuki, "Load characteristics of a spiral inductor type thin film microtransformers," *IEEE Transactions on Magnetics*, pp. 3207–3209, June 1993.

[18] T. Yachi, M. Mino, A. Tago, and K. Yanagisawa, "A new planar microtransformer for use in micro-switching-converters," *IEEE Transactions on Magnetics*, pp. 1969–1973, April 1992.

[19] C. Ahn and M. Allen, "A comparison of two micromachined inductors (bar and meander-type) for fully integrated boost dc/dc power converters," *IEEE Transactions on Power Electronics*, pp. 239–245, March 1996.

[20] Y. Massoud and J. White, "Simulation and modeling of the effect of substrate conductivity on coupling inductance," in *Proceedings of the IEEE International Electron Devices Meeting*, December 1995.

[21] Y. Massoud and J. White, "Simulation of the coupling inductance effect on circuit crosstalk," in *Proceedings of the Techon conference*, September 1996.

[22] Y. Massoud, S. Majors, T. Bustami, and J. White, "Layout techniques for minimizing on-chip interconnect self inductance," in *Proceeding of the IEEE Design Automation Conference*, June 1998.

[23] Y. Massoud, "How does the substrate conductivity affect the on-chip coupling inductance behaviour," in *Proceedings of the MIT Student Workshop on Computing Technology*, August 1996.

106

[24] Y. Massoud and J. White, "Simulating and modeling the effect of substrate conductivity coupling inductance and circuit crosstalk," *To be Submitted to IEEE Transactions on Electron Devices*, 1999.

[25] Y. Massoud, J. Wang, and J. White, "Accurate inductance extraction with permeable materials using qualocation," in *Proceedings of the International Conference on Modeling and Simulation of Microsystems*, April 1999.

[26] Y. Massoud and J. White, "Fast inductance extraction of 3-d structures with non-const permeabilities," in *Proceedings of the International Conference on Modeling and Simulation of Microsystems*, April 1998.

[27] Y. Massoud and J. White, "Fastmag: a 3-d fast inductance extraction program for structures with permeable materials," *To be Submitted to IEEE Transactions on Magnetics*, 1999.

[28] H. A. Haus and J. R. Melcher, *Electromagnetic Fields and Energy*. Englewood Cliffs, NJ: Prentice-Hall, 1989.

[29] M. Kamon, M. J. Tsuk, and J. White, "Fasthenry, a multipole-accelerated 3-d inductance extraction program," in *Proceedings of the ACM/IEEE Design Automation Conference*, (Dallas, TX), pp. 678–683, June 1993.

[30] P. Brennan, N. Raver, and Ruehli, "Three Dimensional Inductance Computations with Partial Element Equivalent Circuits," *IBM Journal of Research and Develop.*, pp. 661–668, November 1979.

[31] L. Greengard, *The Rapid Evaluation of Potential Fields in Particle Systems*. Cambridge, Massachusetts: M.I.T. Press, 1988.

[32] K. Nabors and J. White, "Fastcap: A multipole accelerated 3-D capacitance extraction program," *IEEE Transactions on Computer-Aided Design of Integrated Circuits and Systems*, vol. 10, pp. 1447–1459, November 1991.

[33] D. D. Ling and A. E. Ruehli, *Circuit Analysis, Simulation, and Design 2*. New York: Elsevier, 1988.

[34] E. Adler, J. DeBrosse, S. Geissler, S. Holmes, M. Jaffe, J. Johnson, C. Koburger, J. Lasky, B. Lloyd, G. Miles, J. Nakos, W. Noble, S. Voldman, M. Armacost, and R. Ferguso, "The Evolution of IBM CMOS DRAM Technology," *IBM Journal of Research and Develop.*, pp. 167–188, March 1995.

[35] A. C. Cangellaris, J. L. Prince, and L. P. Vakanas, "Frequency-dependent inductance and resistance calculation for three-dimensional structures in high-speed interconnect systems," *IEEE Transactions on Components, Hybrids, and Manufacturing Technology*, vol. 13, pp. 154–159, March 1990.

[36] C. Trowbridge, "Three dimensional field computation," *IEEE Transactions on Magnetics*, pp. 293–297, January 1982.

[37] W. Rucker, C. Magele, E. Schlemmer, and K. Richter, "Boundary element analysis of 3-d magnetostatic problems using scalar potentials," *IEEE Transactions on Magnetics*, pp. 1099–1102, March 1992.

[38] J. Simkin and C. Trowbridge, "On the use of total scalar potential in the numerical solution of field problems in electrmagnetics," *International Journal for Numerical Methods in Engineering*, vol. 14, pp. 423–440, 1979.

[39] A. Kalimov and M. Svedentsov, "Three-dimensional magnetostatic field calculation using integro-differential equation for scalar potential," *IEEE Transactions on Magnetics*, pp. 667–670, May 1996.

[40] W. Rucker and K. Richter, "Three-dimensional magnetostatic field calculation using boundary element method," *IEEE Transactions on Magnetics*, pp. 23–26, January 1988.

[41] C. Magele, H. Stogner, and K. Preis, "Comparison of different finite element formulations for 3d magnetostatic problems," *IEEE Transactions on Magnetics*, pp. 31–34, January 1988.

[42] L. Han, L. Tong, and J. Yang, "Integral equation method using total scalar potential for the simulation of linear or nonlinear 3d magnetostatic field with open boundry," *IEEE Transactions on Magnetics*, pp. 2897–2900, September 1994.

[43] M. Friedman, "Mathematical study of the nonlinear singular integral magnetic field equation," *Siam Journal of Applied Math.*, vol. 39, no. 1, pp. 14–20, August 1980.

[44] H. Igarashi and T. Honma, "An analysis of thin magnetic materials using hypersingular integral equations," *IEEE Transactions on Magnetics*, pp. 682–685, May 1996.

[45] D. Zheng and K. Davey, "A boundary element formulation for thin shell problems," *IEEE Transactions on Magnetics*, pp. 675–677, May 1996.

[46] K. Sawa and T. Hirano, "An evaluation of the computional error near the boundary with magnetostatic field calculation by b.e.m.," *IEEE Transactions on Magnetics*, pp. 403–406, March 1990.

[47] M. Koizumi, M. Onisawa, and M. Utamura, "Three-dimensional magnetic field analysis method using scalar potential formulated by boundary element method," *IEEE Transactions on Magnetics*, pp. 360–363, March 1990.

[48] S. Babic, B. Krstajic, S. Milojkovic, and Z. Andjelic, "An efficient approcah for the calculation of 3d magnetostatic field of current-carrying regions of typical form," *IEEE Transactions on Magnetics*, pp. 423–426, January 1988.

[49] B. krstajic, Z. Andelic, S. Milojkovic, S. Babic, and S. Salon, "Nonlinear 3d magnetostatic field calculation by the integral equation method with surface and volume charges," *IEEE Transactions on Magnetics*, pp. 1088–1091, March 1992.

[50] S. Babic, Z. Andjelic, B. Krstajic, and S. Salon, "Analytical calculation of the 3d magnetostatic field of a torroidal conductor with rectangular cross section," *IEEE Transactions on Magnetics*, pp. 3162–3164, November 1988.

[51] C. Desoer and E. Kuh, *Basic Circuit Theory*. New York: McGraw-Hill, 1969.

[52] R. F. Harrington, *Field Computation by Moment Methods*. New York: MacMillan, 1968.

[53] J. D. Jackson, *Classical Electrodynamics*. New York: John Wiley & Sons, 1999.

[54] W. T. Weeks, L. L. Wu, M. F. McAllister, and A. Singh, "Resistive and inductive skin effect in rectangular conductors," *IBM Journal of Res. and Develop.*, vol. 23, pp. 652–660, November 1979.

[55] A. E. Ruehli, "Inductance calculations in a complex integrated circuit environment," *IBM J. Res. Develop.*, vol. 16, pp. 470–481, September 1972.

[56] M. Kamon, M. Tsuk, and J. White, "Fasthenry: A mutipole-accelerated 3-d inductance extraction program," *IEEE Transactions on Microwave Theory and Techniques*, pp. 1750–1758, September 1994.

[57] F. W. Grover, *Inductance Calculations, Working Formulas and Tables*. New York: Dover Publications, 1962.

[58] J. N. Newman, "Distributions of sources and normal dipoles over a quadrilateral panel," *Journal of Engineering Mathematics*, vol. 20, no. 2, pp. 113–126, 1986.

[59] J. Hess and A. Smith, "Calculation of non-lifting potential flow about arbitrary three-dimensional bodies," *Report No. E. S. 40622, Douglas Aircraft Comany, Long Beach, CA*, 1962.

[60] Y. Liu, "Analysis of shell-like structures by the boundary element method based on 3-d elasticity: formulation and verification," *International Journal for Numerical Methods in Engineering*, vol. 41, pp. 541–558, 1998.

[61] Y. Liu, "Aanalysis of two-dimensional thin structures(from micro to nano-scales) using the Boundary Element Method," *Submitted to Computational Mechanics*, 1998.

[62] D. Z. Y. Liu and F. Rizzo, *Nearly singular and hypersingular integrals in the boundary element method: in C. Brebbia et.al., Boundary Elements XV*. Worcester, MA: Computational Mechanics Publications, 1993.

[63] D. Engels, *Numerical Quadrature and Cubature*. New York: Academic Press, 1980.

[64] J. Tausch and J. White, "Second kind integral formulations of the capacitance problem," *Adv. Comput. Math.*, vol. 9, pp. 217–232, 1998.

[65] J. Wang, J. Tausch, and J. White, "Improved integral formulations for fast 3-d method-of moments solvers," in *Proceedings of EPEP*, October 1998.

[66] D. Chen, J. Brug, and R. Goldfarb, "Demagnetizing Factors for Cylinders," *IEEE Transactions on Magnetics*, pp. 3601–3619, July 1991.

[67] R. I. Joseph, "Ballistic demagnetizing factor in uniformly magnetized cyliners," *Journal of Applied Physics*, pp. 4639–4642, December 1966.

[68] R. I. Joseph and E. Schlomann, "Demagnetizating field in nonellipsoidal bodies," *Journal of Applied Physics*, pp. 1579–1593, May 1965.

[69] M. Sato and Y. Ishii, "Simple and approximate expressions of demagnetizing factors of uniformly magnetized rectangular rod and cylinder," *Journal of Applied Physics*, pp. 983–985, July 1989.

[70] R. Bozorth and D. Chapin, "Demagnetizing factors of rods," *Journal of Applied Physics*, pp. 320–326, 1942.

[71] R. Bozorth, *Ferromagnetism*. IEEE Press, 1993.

[72] R. Rodriquez, J. Dishman, F. Dickens, and E. Whelan, "Modeling of two-dimensional spiral inductors," *IEEE Transactions on Components Hybrids and Manufacturing Technology*, pp. 535–541, December 1980.

[73] N. Saleh, "Variable microelectronic inductors," *Electronics Letters*, pp. 118–12, March 1970.

[74] W. Roshen and D. Turcotte, "Planar inductors on magnetic substate," *IEEE Transactions on Magnetics*, pp. 3213–3216, November 1988.

[75] W. Roshen and D. Turcotte, "Effect of finite thickness of magnetic substrate on planar inductors," *IEEE Transactions on Magnetics*, pp. 270–275, January 1990.

[76] G. H. Golub and C. F. V. Loan, *Matrix Computations*. Baltimore: The Johns Hopkins University Press, 1989.

[77] J. Stoer, *Introduction to Numerical Analysis*. New York: Springer Verlag, 1980.

[78] L. Trefethon and D. Bau, *Numerical Linear Algebra*. Philadelphia: Siam Socity for Industrial and Applied Mathematics, 1997.

[79] Y. Saad and M. H. Schultz, "GMRES: A generalized minimal residual algorithm for solving nonsymmetric linear systems," *SIAM Journal on Scientific and Statistical Computing*, vol. 7, pp. 856–869, July 1986.

[80] L. Daniel, C. Sullivan, and S. Sanders, "Design of Microfabricated InductorsD," *IEEE Transactions on Power Electronics*, vol. 14, July 1999.